Isotopic production cross sections of spallation-evaporation residues from reactions of ^{238}U(1*A* GeV) with deuterium

E. Casarejos,[1,*] J. Benlliure,[1] J. Pereira,[1] P. Armbruster,[2] M. Bernas,[3] A. Boudard,[4] S. Czajkowski,[5] T. Enqvist,[2] R. Legrain,[4] S. Leray,[4] B. Mustapha,[3] M. Pravikoff,[5] F. Rejmund,[3] K.-H. Schmidt,[2] C. Stéphan,[3] J. Taieb,[3] L. Tassan-Got,[3] C. Volant,[4] and W. Wlazlo[4]

[1]*Universidade de Santiago de Compostela, E-15782 Santiago de Compostela, Spain*
[2]*Gesellschaft für Schwerionenforschung, D-64291 Darmstadt, Germany*
[3]*Institute de Physique Nucléaire, F-91406 Orsay cedex, France*
[4]*DAPNIA/SPhN, CEA/Saclay, F-91191 Gif sur Yvette cedex, France*
[5]*CENBG, F-33175 Gradignan cedex, France*

(Received 14 March 2006; published 23 October 2006)

Isotopic production cross sections and momentum distributions of 602 residual nuclei produced in the collision of ^{238}U(1*A* GeV) with deuterium have been measured. These data are relevant for a better understanding of spallation reactions for use as neutron sources for accelerator-driven systems or to produce radioactive nuclear beams. Access to primary residue production makes it possible to study the main reaction mechanisms involved: intranuclear cascade, particle evaporation, and fission. The characteristics of the reaction investigated and the high fissility of the ^{238}U and the dinucleon projectile system are discussed and compared with other available experimental data.

DOI: 10.1103/PhysRevC.74.044612 PACS number(s): 25.70.Mn, 25.75.−q, 25.40.Sc, 25.70.Kk

I. INTRODUCTION

In this work we present the production cross sections of residual nuclei after spallation-evaporation of ^{238}U(1*A* GeV) induced by deuterium. The spallation-fission residue results will be presented in an independent paper [1]. This study is part of a large experimental program performed at GSI to determine the production cross sections of residual nuclei in spallation reactions [2–12]. The purpose of this project was to study the main reaction mechanisms involved in processes of this type, and to establish a large benchmark data collection. The initial goal of the program was to provide relevant nuclear data for the design of accelerator-driven reactor systems (ADS) [13,14] and spallation-neutron sources and for the production of radioactive ion beams [15].

A fundamental requirement for these applications is a precise knowledge of the residual nuclei produced in spallation reactions. The residual production cross sections of these nuclei will define the radioactive inventory on the target for spallation-neutron sources and the intensities of radioactive nuclear beams produced in future facilities. In addition, the isotopic production cross sections of residual nuclei in spallation reactions are an optimum observable for characterizing the dynamics of hot nuclei. These reactions are understood as a two-step process [16]: collisions induce the rapid formation of an excited target prefragment, which then deexcites, by particle emission and/or fission. This leads to either a spallation-evaporation or spallation-fission residue. The final distribution of reaction residues is determined by the isotopic nature of the prefragments, together with their excitation energy and angular momentum, all of which influence the subsequent deexcitation stage.

Experimental investigations of spallation residues using direct kinematics are limited by the low recoil velocity of the target residues. For this reason, mainly radiochemical or spectroscopic techniques have been used to determine the nature of the residual nuclides produced in these reactions [17,18]. However, with these techniques, only the isobaric production of the residues after their β decay can be determined. Primary isotopic productions can be measured for only a few shielded isotopes.

The alternative experimental approach followed in this work, based on the inverse-kinematic technique, makes it possible to overcome most of the limitations of the direct method. Using this approach, the residual nuclei, which fly forward, preserve the kinetic properties of the projectile and can be identified by using a magnetic spectrometer [19]. The short time required for this measurement ensures the observation of the primary production of the residues before β decay. In the experiment, we present in this paper, the magnetic spectrometer fragment separator (FRS) at GSI-Darmstadt and a specific detection setup made possible the separation and isotopic identification of all residues after the fragmentation of a ^{238}U beam at 1*A* GeV in a deuterium target.

In this work, we describe the technique used to achieve the resolution required for the complete mass and atomic-number identification of the spallation-evaporation residues. This unambiguous identification makes it possible to determine the isotopic production cross sections and longitudinal momentum distributions. We studied the fragmentation of ^{238}U, the heaviest stable nucleus that can be accelerated and that is characterized by a high fissility. A specially designed cryogenic target [20] was used to investigate deuteron-induced collisions. Deuterium is the next step after single-nucleon induced collisions. It also presents a wide spatial distribution of nuclear matter. The study of this reaction is expected to provide

*Electronic address: casarejo@usc.es

key information about more complex collisions induced by multinucleon targets.

A detailed explanation of the experimental method is given in Sec. II. In Sec. III, we present the main results of our work: the production cross sections of the residues and their momentum distributions. The data presented here will be compared in Sec. IV with similar measurements of other systems in order to discuss the relevant reaction mechanisms that govern the measured productions.

II. EXPERIMENTAL TECHNIQUE

The experiment was performed at GSI-Darmstadt by shooting a ^{238}U beam, accelerated in the Schwerionen-Synchrotron (SIS) up to 1A GeV, onto a cryogenic target filled with deuterium. The liquefied deuterium (below 20 K), with a mass thickness of 200 mg/cm^2, was encapsulated in a container with Ti windows (total thickness 36.32 mg/cm^2) and surrounded by Mylar-Al (9.7 mg/cm^2) for thermal isolation. A second target, with the same components and thicknesses as the container, was used to determine the additional production of residual nuclei in the windows of the cryogenic target. The beam intensity, up to 10^7 particles/s, was measured continuously by a secondary-electron transmission monitor (seetram) [21]. This device was carefully calibrated [22] in the time course of the experiment to ensure accuracy in the normalization of the measurements. The dead time of the acquisition, typically below 20%, was also monitored continuously.

Good resolution in the separation and identification of the heavy residues, $A/\Delta A \sim 400$ for $A \sim 238$, is experimentally very demanding and only possible with a high-resolving-power magnetic spectrometer like the fragment separator [23]. This is a 70 meter long, zero-degree magnetic spectrometer with an angular acceptance of 15 mrad around the central trajectory, a longitudinal momentum acceptance of 3%, and a nominal resolving-power value of 1500. The FRS was used in its achromatic mode. Figure 1 provides a schematic view of the FRS setup used in this experiment. Among the many magnetic elements, only the dipole magnets are shown. The highly symmetric layout of the spectrometer is easily seen.

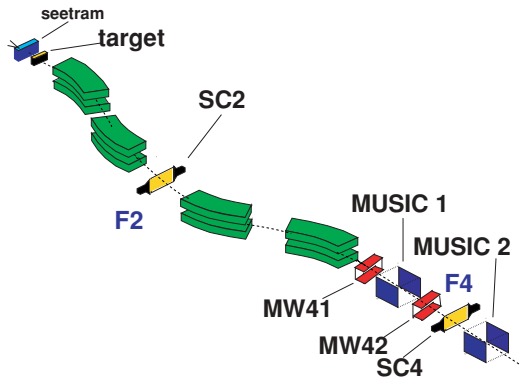

FIG. 1. (Color online) Schematic representation of the FRS, where only the dipole magnets and main detectors are depicted. The intermediate (F2) and final (F4) focal planes are indicated. The energy degrader was placed just after the plastic scintillator SC2.

The residual nuclides, retaining the kinematic properties of the projectile, flew forward through the FRS and were identified in mass and atomic numbers by a specialized detector setup (Fig. 1). The short times of flight, below 300 ns, allowed us to observe the primary production from the fragmentation reaction. Only a few extremely short-lived α emitters with 128 neutrons, having half-lives of around 100 ns, partially decayed inside the spectrometer. The production cross sections of all other nuclides were determined prior to their radioactive decay.

The FRS separates the nuclear fragments according to their magnetic rigidity $B\rho = p_L/Q = Auc\beta\gamma/Qe$, with p_L being the longitudinal momentum, A the mass number, Q the ionic charge, u and e the atomic mass and charge units, respectively, c the speed of light, and β and γ the relativistic parameters. The measurement of the position of the fragments in the magnetic dispersion coordinate x at the intermediate and final focal planes of the FRS (F2 and F4 in Fig. 1) defines the magnetic rigidity $B\rho$ of each residue according to $\Delta B\rho = \Delta x/D$, where D is the dispersion, and $\Delta B\rho$, Δx are the differences in rigidity and position, respectively, with respect to a nucleus that follows the central trajectory along the FRS. The positions were determined with two plastic scintillators [24], one placed at the intermediate focal plane of the FRS (SC2) and another at the final focal plane (SC4), about 2 m beyond the end of the FRS vacuum pipe. Additionally, the drift times measured with the multisampling ionization chambers (MUSIC) [25] were used to define the tracking angle. The position calibration of the plastic scintillators was done with multiwire proportional chambers (MW) placed next to the plastic scintillators and independently calibrated. The values of the dispersion D and the dipole radii ρ were calibrated using the primary beam and its charge states. The magnetic fields B of the FRS were determined by Hall probes. The final resolution (full width at half maximum, FWHM) obtained in the present experiment for $\Delta B\rho/B\rho$ was 4×10^{-4}.

The time-of-flight (TOF) was also measured using the two plastic scintillators placed at the focal planes, which determined the relativistic reduced momentum $\beta\gamma$. The TOF calibration was obtained by passing the beam through the FRS at different energies. This procedure also made it possible to calibrate both the thicknesses of the layers of matter placed along the FRS and the length of the flight path for the central trajectory along the second half of the FRS, about 35 m. The length of all other trajectories was corrected according to the tracking angle measured with the MUSIC chambers at the FRS exit. The use of different detectors guaranteed a detection efficiency higher than 99% for the rates observed during the experiment, which were typically a few 10^3 particles per second.

The separation and isotopic identification of the residues produced in the reaction that we studied is extremely challenging. The contribution of different charge states must be taken into account, as it affects the separation in magnetic rigidity as well as the atomic-number identification using the ionization chambers. To overcome this obstacle, we used the momentum-loss achromat technique [26], which relies on the use of an achromatic degrader to improve the separation of heavy residues. A combined measurement of

the energy loss of the residues in the intermediate degrader and in two ionization chambers allowed us to separate the contributions from the different charge states [27]. Since the contamination due to charge states decreases with the atomic number we applied the two different methods described below to identify residues with Z above and below 70.

A. Isotopic identification of residues with $Z < 70$

Elements were identified by measuring the energy loss ΔE with MUSIC chambers placed at the exit of the FRS. The measured energy-loss value was corrected for ion velocity dependence, ion-recombination in the gas, and border effects of the electric field. Figure 2(a) shows a typical ΔE spectrum after corrections and charge calibration, measured with one MUSIC chamber, at various FRS settings. The beam signal was used as a reference to identify the different atomic charges. For elements with Z below 70 and energies above 800A MeV, the energy loss measured with one MUSIC chamber made it possible to determine the atomic charge with a resolution better than 7×10^{-3} (FWHM).

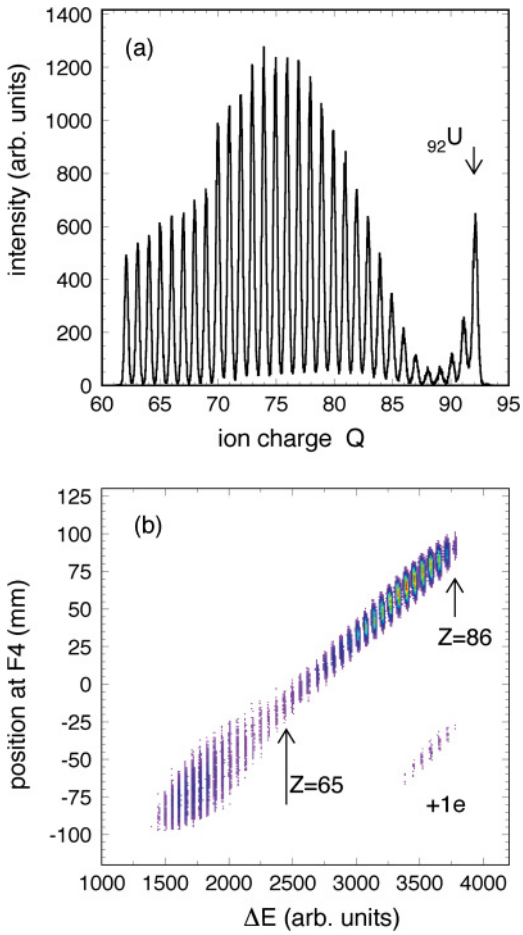

FIG. 2. (Color online) (a) Energy loss measured with one MUSIC chamber, corrected for velocity and horizontal position dependences inside the chambers, and calibrated to reproduce the ionic charge Q. Beam value is indicated. (b) Position measured in the dispersion coordinate at the FRS exit (F4) vs energy loss measured by one ionization chamber, in arbitrary units. Two elements are marked. We can observe how the charge resolution allows us to clearly separate elements with Z below ~70. The band just below the most populated area corresponds to those nuclides carrying one electron in the second stage of the FRS. These residues were transmitted in one FRS magnetic setting centered on ^{180}Re.

While the contamination of charge states for elements with Z below 70 is expected to be smaller than 1%, this contribution increases very fast with Z. One part of the charge states present can be suppressed using the procedure shown in Fig. 2(b): the dispersion coordinate at F4 vs the ΔE measured in one MUSIC chamber, in this case for all the residues transmitted in one FRS magnetic setting centered on ^{180}Re. The dependence of the position at F4 on the charge state of the transmitted ions enabled the separation of the different charge state contributions in one stage of the FRS. It is worth noting that the population of nonbare ions decreases drastically for elements below $Z = 70$. In that Z region, the ambiguity of the charge state disappears since the ions are fully stripped (with a probability higher than 99%), and the resolution in charge is rather good. The selection of only fully stripped ions, and the A/Q value measured with both $B\rho$ and TOF, made it possible to construct an identification matrix, like the one shown in Fig. 3. Each spot in this matrix corresponds to a different nuclide, measured in one FRS magnetic setting centered around ^{165}Re. The resolution in mass separation was better than $A/\Delta A \sim 325$ (FWHM) for $A = 160$. Residues with Z values below 70 covered a $B\rho$ range between 12.079 and 14.346 Tm. According to the FRS acceptance, 14 magnetic settings were needed to measure all the momentum distributions and production cross sections of the spallation-evaporation residues in that range of elements.

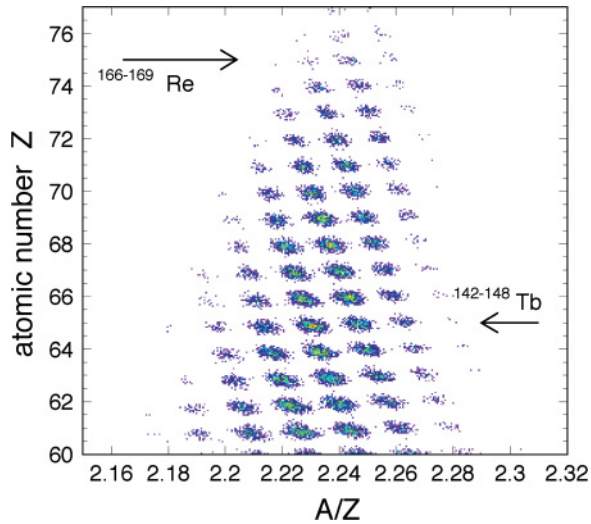

FIG. 3. (Color online) Scatter plot of the atomic number Z value obtained from the energy loss measured with the MUSIC chambers, as a function of the A/Z value deduced from the magnetic rigidity and the TOF measurements, for a magnetic setting of the FRS centered in $^{165}_{75}$Re. Each spot corresponds to a single nuclide. Some isotopes of $_{65}$Tb and $_{75}$Re are indicated.

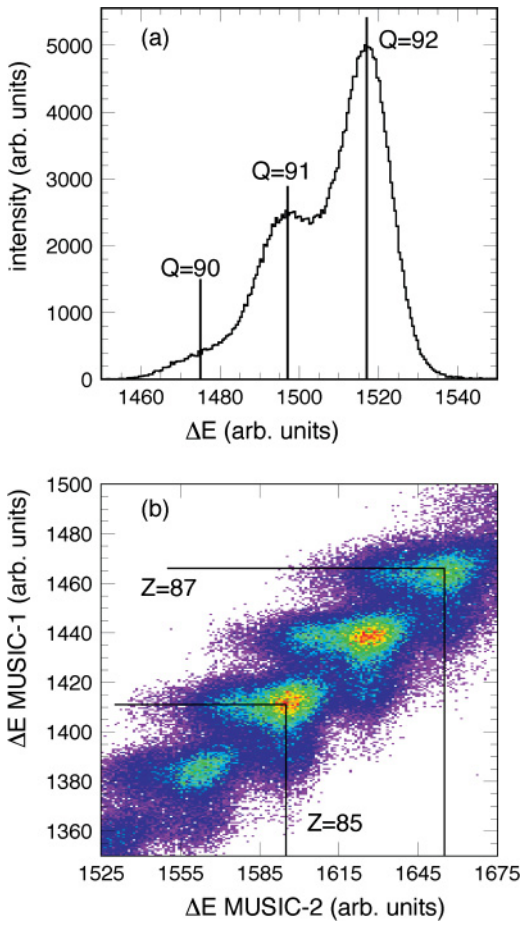

FIG. 4. (Color online) (a) Energy loss measured with one MUSIC chamber for the ^{238}U beam with an energy of about 600A MeV. Three bumps in the distribution correspond to three charge states populated by the beam. Corresponding average position of charges 90–92 are marked. (b) Scatter plot of energy loss measured in two ionization chambers. Spots correspond to atomic charges 84–87, the mean position is indicated for values 85 and 87.

B. Isotopic identification of residues with $Z \geqslant 70$

As previously commented, the identification of heavy residues is a challenging experiment. Two issues must be overcome to obtain an unambiguous identification of residues with Z above 70: contamination due to charge states produced inside the FRS, and the loss in resolution in ΔE measurements with the MUSIC chambers due to stochastic charge-state changes within the gas. The method adopted here used a profiled aluminum achromatic energy degrader, placed at the intermediate focal plane of the FRS, and the measurement of energy losses in two MUSIC chambers, combined adequately.

The two problems are illustrated in Fig. 4(a). Energy loss was measured with a MUSIC chamber for ^{238}U ions at the exit of the FRS with an energy of about 600A MeV, after traversing the energy degrader. Fully stripped ions, hydrogen- and helium-like ionic states, contribute to the spectrum. Two niobium stripper foils were installed behind the target (60 mg/cm^2) and at the intermediate focal plane of the FRS (105 mg/cm^2). These foils limited the number of ionic charge states possible inside the spectrometer, thus enhancing the population of fully stripped ions. We can also notice in Fig. 4(a) that the resolution in charge separation was insufficient for an unambiguous identification. We used the independent measurements of two MUSIC chambers to correctly determine the atomic numbers. The energy losses ΔE measured were also corrected for velocity and position dependences. For each ion, we defined a new value $Q_{\mathrm{eff}}^{\mathrm{max}}$ which corresponds to the highest energy loss measured by any of the two chambers. Since $\Delta E \propto Q^2$, the value of $Q_{\mathrm{eff}}^{\mathrm{max}}$ is sensitive to changes of the ionic charge between the two chambers. The probability of one ion being fully stripped in at least one chamber was optimized with a Nb foil (230 mg/cm^2) placed between the two chambers. Thus $Q_{\mathrm{eff}}^{\mathrm{max}}$ corresponds to Z with a maximal probability. The ion could only be misidentified if it kept at least one electron as it passed through the two chambers. The probability of this happening is about 17% for U isotopes and decreases with Z to 1% for Yb isotopes. This method is shown in Fig. 4(b), representing the scatter plot of ΔE measured in the two chambers using arbitrary units. Each group corresponds to one atomic number, some of which are indicated. The characteristic double-wing shape is the result of the ionic charge distribution measured in each chamber. With any observed ΔE values, $Q_{\mathrm{eff}}^{\mathrm{max}}$ can be defined once the observed main diagonal of charges has been established.

Although the method significantly improves the situation, the probability of misidentification is still high, and the resolution in charge separation remains limited.

To clarify the ambiguities in element identification using two MUSIC chambers, we incorporated the additional information provided by the degrader, which improved the charge resolution and the separation of the different charge states within the FRS. The energy loss of one ion in the degrader is given by $(\gamma_1 - \gamma_2)Au$, with γ the relativistic factor, 1 and 2 represent the first (until F2) and second (until F4) stages of the FRS, respectively, and A is the mass number of the ion. We defined an alternative magnitude $\Delta E_d = (\gamma_1 - \gamma_2)uA/Q$, which is sensitive to changes in the atomic charge of the ion within the FRS. Both γ_2 and the ratio A/Q are determined in the second stage of the FRS, using the $B\rho$ and TOF values. Assuming that A/Q is the same in both stages of the FRS, the $B\rho$ value can be determined in the first stage, thus giving the values of γ_1 and ΔE_d.

In Fig. 5, we plotted ΔE_d (in arbitrary units) vs $Q_{\mathrm{eff}}^{\mathrm{max}}$ (calibrated in atomic number) for a magnetic setting centered around ^{195}Pb. The spots lie in three tilted parallel lines. The most populated spots, in the central tilted line, correspond to those nuclides which are bare along the spectrometer. The spots above the most populated ones correspond to those nuclides with one electron before the degrader and bare after; those below, to nuclides bare before the degrader and with one electron after. A nuclide that keeps one electron along the FRS but is fully stripped in one of the chambers will lie on the smaller spots next to the main ones, marked as $+1e$. Those $+1e$ spots are also populated by nuclides which carried one electron in both ionization chambers, but were fully stripped within the FRS. The most unfavorable case in our setup is that of a nuclide with one (or two) electron(s) unchanged along the entire setup line. The identification procedure would then fail in the assignation of both Q and Z, and, consequently, A.

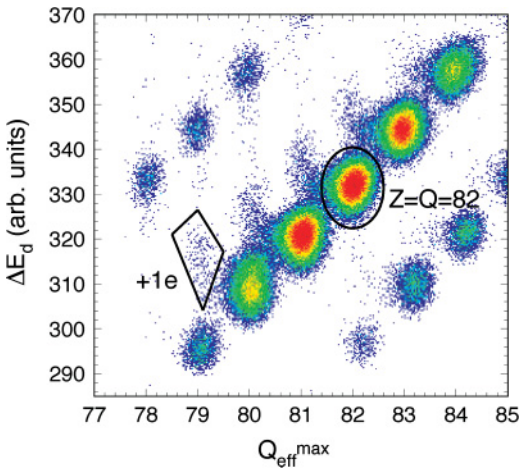

FIG. 5. (Color online) Scatter plot of energy loss in the intermediate degrader ΔE_d as a function of energy loss, calibrated in charge, measured with two ionization chambers $Q_{\rm eff}^{\rm max}$. The FRS magnetic setting was centered around $^{195}_{82}$Pb. The most populated spots correspond to those nuclides that are bare along the spectrometer. The element $Z = 82$ is indicated. Spots above the most populated ones correspond to nuclides with one electron before the degrader and bare after; those below, to nuclides bare before the degrader and with one electron after. The case corresponding to a nuclide with one electron unchanged all along the FRS path, indicated as $+1e$, is also separated in the less populated spots near the main line.

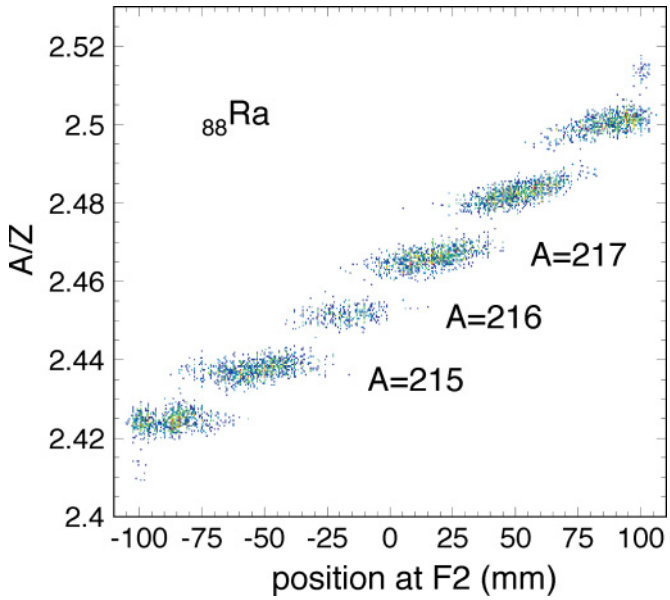

FIG. 6. (Color online) Scatter plot of A/Z obtained from the magnetic rigidity and the TOF measurements, as a function of the position of the dispersion coordinate at the intermediate FRS focal plane (F2). The FRS magnetic setting was centered around the nuclide ^{216}Ra, with the selection $Q = Z = 88$.

Fortunately, according to our estimations, these events amount to less than 1% even in the least favorable case of ^{238}U.

In our analysis, we used only those events corresponding to fully stripped ions ($Z = Q$) along the setup, with both Z and Q clearly defined. The drawback of this method is the thickness of the degrader, which corresponds to approximately 50% of the range of the residues: 4189.5 mg/cm^2 for residues with Z from 70 to 75 and from 85 to 92; 4618.8 mg/cm^2 for residues with Z from 75 to 85. Such thicknesses reduce the number of nuclides accepted in a single magnetic setting to about 20 [26] and induce secondary reactions. The residues with Z above 70 covered a $B\rho$ range between 12.386 and 14.558 Tm. According to the FRS acceptance and the degrader selection, more than 50 FRS magnetic settings were needed to scan the momentum distribution of all the nuclides. On the other hand, this method provides an unambiguous pattern of charge assignation and an improved resolution for separating the different elements. It also allowed us to adjust the beam intensity to the specific production cross sections in a restricted region of nuclides. These advantages largely overcome all related drawbacks, making this a valuable and high-quality technique.

Figure 6 shows the measured A/Z ratio for some isotopes of Ra vs the positions measured for the dispersion coordinate at the intermediate FRS focal plane, measured in a magnetic setting centered around ^{216}Ra. The A and Z values were obtained with the $B\rho$ and TOF measurements. The selection of fully stripped ions was obtained as described previously. Here we see the quality of the final isotopic separation that has been obtained using this procedure, resulting in an unambiguous identification of the isotopes. The degrader is the key element in the identification of heavy nuclides, since it allows the unambiguous separation of the different ionic charge states of a nucleus. The resolution achieved in this case is typically $A/\Delta A \sim 330$ (FWHM) for $A = 215$, and $Z/\Delta Z \sim 160$ (FWHM) for $Z = 88$.

III. PRODUCTION CROSS SECTIONS

The final production cross section $\sigma(r)$ of the different projectile residues $r = (Z, A)$ were obtained from the production yields $y(r)$ normalized to the number of atoms per surface unit of the target μ and the beam intensity N_b. The limited longitudinal momentum acceptance of the FRS determined both the range of isotopes and the range of momentum observed in one magnetic setting of the spectrometer. Most of the residues were measured in different magnetic settings, each one covering a part of their momentum distribution. By overlapping consecutive settings, we could measure the entire momentum distribution of all residues. Figure 7 shows the momentum distribution p_L in the projectile frame for the nuclide ^{160}Yb. The four different areas correspond to normalized data recorded in different magnetic settings, each contributing to the reconstruction of the whole momentum distribution.

The measured yields y_m, evaluated from the complete momentum distributions, had to be corrected for the different effects inherent in our experimental method and data analysis. The corrections included the angular acceptance of the FRS $f_{\rm acc}$, the selection of atomic charge states f_q, the losses by secondary reactions in the different layers of matter along the FRS $f_{\rm loss}$, the dead time f_τ of the data acquisition system, and the additional production of residual nuclides $y_{\rm tar}$ in the target windows. Since some light residues can be produced either

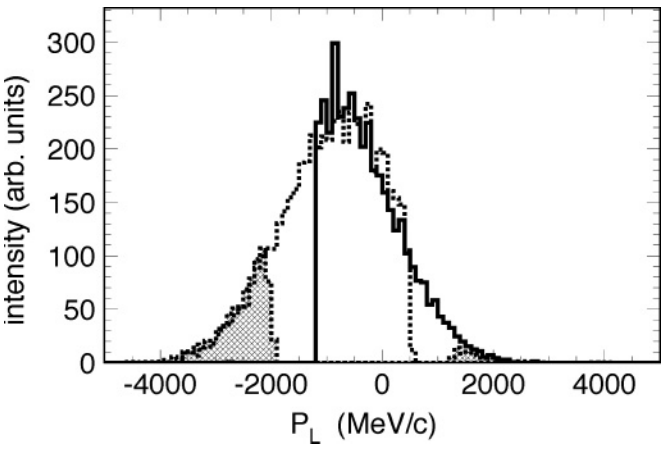

FIG. 7. Longitudinal-momentum distribution p_L, in the frame defined by the projectile in the middle of the target, for the nucleus $^{160}_{70}$Yb, produced in the reaction ^{238}U(1A GeV) + d. The different areas correspond to the momentum intervals measured in different FRS magnetic settings. Overlapping these different measurements allows us to reconstruct the whole momentum distribution.

by evaporation or fission processes, an additional correction factor $f_{\rm evap}$ provided the fraction of evaporation events. The final yield of a residue was thus defined as

$$y(r) = f_{\rm acc}(r) f_q(r) f_{\rm loss}(r) f_\tau f_{\rm evap}(r) [y_m(r) - y_{\rm tar}(r)] . \quad (1)$$

Finally, the measured cross sections were also corrected for the multiple reactions that take place inside the target. In the following section, we will discuss in detail all the corrections applied to define the yields and the procedure for evaluating the final isotopic cross sections along with any associated uncertainties.

A. Yield corrections

We have explained how the limited longitudinal momentum acceptance of the FRS was overcome by overlapping different magnetic settings. However, the measured yields also have to be corrected from the limited angular acceptance of the spectrometer [28]. For all the residues we studied, with a mass number above 130, that were produced by spallation-evaporation, the angular transmission was estimated to be higher than 99% [$f_{\rm acc}(r) \sim 1$] with an accuracy within 3%.

Since we selected only fully stripped ions, we had to correct the measured yields from the contributions of different charge states all along the FRS as well as within the two ionization chambers. In our case, there were mainly bare, hydrogen- and helium-like atomic states. The correction factor f_q is defined as the inverse of the survival probability of obtaining bare ions through our setup [29]. Figure 8(a) shows f_q applied to the measured yields, as a function of the atomic number Z. The shift at $Z = 70$ occurs because the degrader was not used for the lighter elements. The dispersion of the values for a given Z is due to the mass dependence of the atomic charge distribution. In some cases, we could also measure the ionic charge-state distributions of residues behind the degrader (Fig. 5) and behind the Nb foil placed between the two ionization chambers [Fig. 4(b)]. These direct measurements allowed us to cross-check our calculations of f_q and the associated uncertainty that we estimated to be 5%.

The reactions in the different layers of matter along the path of the ions through the setup attenuated the measured yields. The setup and the identification method guaranteed that this secondary production would not contaminate any other residue. The final survival probability of traversing all the materials $1/f_{\rm loss}$ is the product of the single survival probability in each material (i), evaluated according to the corresponding total reaction cross section σ_i^T, and the material thickness μ_i: $f_{\rm loss} = \prod_i \exp(-\mu_i \sigma_i^T)$. Both nuclear and electromagnetic-dissociation (EMD) processes have been considered in the evaluation of the total reaction cross section. The nuclear process was evaluated with microscopic Glauber-type calculations [30,31]. The EMD contribution was calculated considering the virtual photon field of the target nucleus and the photon absorption cross section of the projectile [32,33]. In Fig. 8(b) we plot the applied correction $f_{\rm loss}$ as a function of the atomic number. The shifts observed in the trend are due to the change in the degrader thickness used in our setup, which was adjusted according to the range of the measured residues. The losses in the degrader amounted to over to 40% for the heavier residues. The reaction cross sections evaluated for these processes have an accuracy within 10%, which we estimated from the scarce data we found for high-energy reactions induced by heavy nuclei. We also cross-checked the accuracy of the evaluation by comparing both the losses of the beam in the plastic scintillator installed in the intermediate focal plane of the FRS, as well as from the comparison of the yields measured with and without the degrader.

In the previous section, we discussed the two different methods for identifying a residue according to its atomic number. The validity and coherence of the two methods can be cross-checked by comparing data analyzed using both techniques in a region of residues where both methods can be applied, such as residues with an atomic number around 70. At the same time, this comparison shows the accuracy of the corrections applied, namely for f_q and $f_{\rm loss}$, due to the presence or absence, of the degrader. In Fig. 9, we present the cross sections measured with degrader σ_d (full symbols) and without degrader $\sigma_{\rm nd}$ (open symbols) of different Re and Yb isotopes. The lower panels show the relative difference $(\sigma_{\rm nd} - \sigma_d)/\sigma_d$. Most of the measured values of $\sigma_{\rm nd}$ and σ_d for residues close to $Z = 70$ were compatible within 10%, which is the limit for the accuracy of the corrections we applied for comparing the results. Very neutron-rich or neutron-deficient isotopes, as well as those with higher charges, showed increasing discrepancies, which are explained by the contamination induced by different charge states that cannot be completely suppressed in the measurements without the degrader.

The dead time of the whole data acquisition system was continuously monitored with an accuracy within 2%, and typical values of about 20%.

The additional production of residual nuclides in the Al-Ti windows of the target container $y_{\rm tar}$ had to be subtracted from the measured yields. To optimize the experimental and analysis efforts, this correction was evaluated with accurate calculations and cross-checked with direct measurements. The production

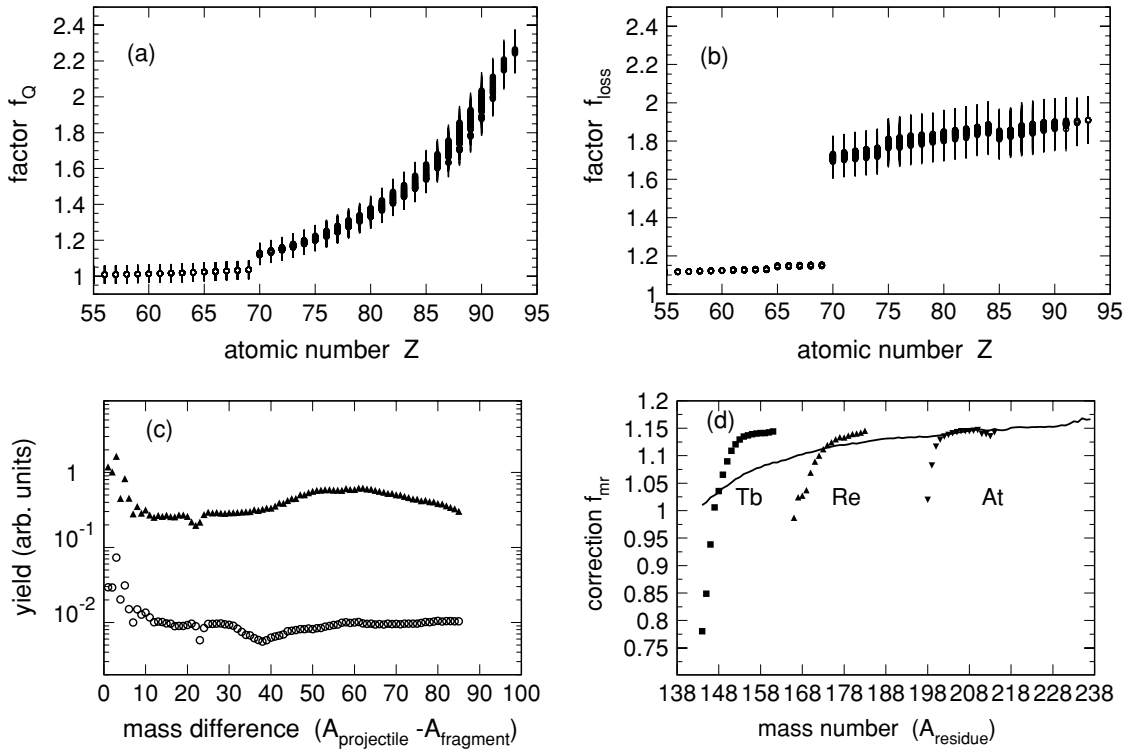

FIG. 8. Corrections applied to the measured yields. (a) Correction factor f_q, inverse of the survival probability of fully stripped ions through the FRS and the ionization chambers, as a function of atomic number. Dispersion of values is due to mass dependence. The shift below $Z = 70$ corresponds to the settings without the degrader. (b) Correction factor $f_{\rm loss}$, inverse of the survival probability to reactions of ions in all layers of matter along the FRS to the ionization chambers, as a function of atomic number. Shifts are due to the change in the degrader thickness, adjusted to the range of residue nuclides. For Z below 70, the degrader is not used. (c) Isobaric distribution of yields for the total target assembly (triangles) and for a deuterium-free target container (circles). Deuterium production is typically 97% of total production. (d) Correction factor $f_{\rm mr}$, ratio of the primary to multiple reaction production within the target, plotted as a function of the mass number of the residue. Line corresponds to the average value weighted by each isobar production. Symbols are the isotopic values of $f_{\rm mr}$ for elements $_{65}$Tb, $_{75}$Re, $_{85}$At.

cross sections of all the residues from the beam impinging in the different layers of the empty target were obtained from model calculations done with the abrasion-ablation Monte Carlo code ABRABLA [34,35]. The production yields of some residual nuclides were directly measured by using an empty target container and following the same analysis method as for deuterium. These values confirmed the adequacy of the calculated production yields in the target window $y_{\rm tar}$. Figure 8(c) shows the isobaric distributions of the measured yield with the whole target (triangles) and the evaluated yields of the empty-target $y_{\rm tar}$ (circles). The production associated with the target windows was, on average, 3% of the total

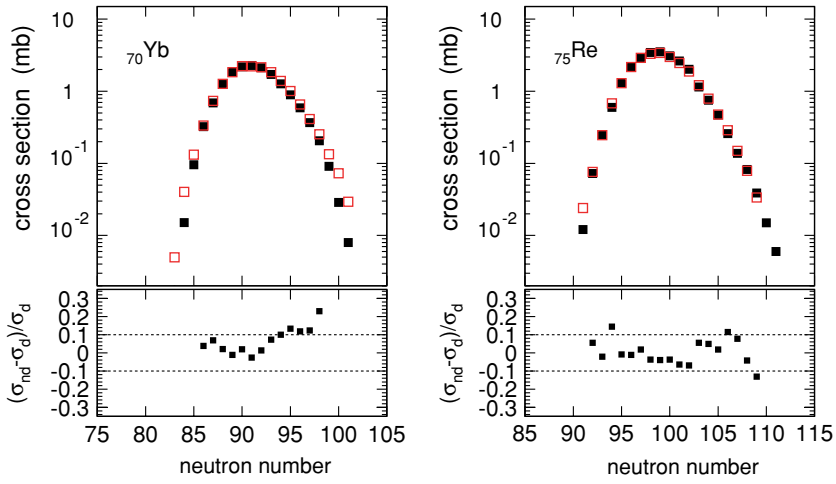

FIG. 9. (Color online) Isotopic production cross sections of residues of $_{75}$Re and $_{70}$Yb as measured with (full symbols) and without (open symbols) degrader. Lower panels show the relative differences of these values.

and never exceeded 10%. A conservative uncertainty factor of 2 assigned to the evaluated $y_{\rm tar}$ resulted in a rather low uncertainty (<6% for 90% of the data) in the final cross sections.

B. Multiple reactions and cross-section definition

To determine the cross section $\sigma(r)$ of each isotope $r = (Z, A)$ from the corrected yields $y(r)$, multiple reactions within the target must be taken into account. In this section, we explain the method we used to evaluate the ratio $f_{\rm mr}$ between the apparent cross section $\sigma_0(r)$ and the real cross section $\sigma(r) = f_{\rm mr}(r)\sigma_0(r)$. The apparent cross section is obtained as the thin-target approximation: $\sigma_0(r) = y(r)/\mu N_b$, with N_b being the beam intensity and μ the target thickness. We estimated that the probability of producing residues by more than two sequential reactions was negligible. Therefore, we considered only residues produced in primary y_1 and secondary y_2 collisions.

Each term y_i is the result of a set of differential equations. The production y_1 can be calculated as

$$y_1(r) = \sigma(r)N_b \frac{\exp\left(-\mu\sigma_b^T\right) - \exp\left(-\mu\sigma_r^T\right)}{\sigma_r^T - \sigma_b^T}, \qquad (2)$$

where σ_b^T and σ_r^T refer to the total reaction cross sections of the beam particles b and residues r with deuterium. Assuming the condition $|\sigma_b^T - \sigma_r^T|\mu \ll 1$, one can approximate

$$y_1(r) \approx \mu N_b \sigma(r) \exp\left[\frac{-\left(\sigma_b^T + \sigma_r^T\right)\mu}{2}\right]. \qquad (3)$$

The values of σ^T were evaluated as explained in Sec. III A. In our setup, we have typical values of $|\sigma_b^T - \sigma_r^T| \sim 500$ mb, and $\mu \sim 6 \times 10^{-5}$ mb^{-1}. If y_1 were the only source of the observed residues, then $f_{\rm mr} = \exp\left[(\sigma_b^T + \sigma_r^T)\mu/2\right]$. Note that this term describes the attenuation of the fluxes of both the beam particles and the residues in the target, as if the reaction had taken place in the middle of the target. If those attenuations are neglected, i.e., $\sigma_b^T \approx \sigma_r^T \approx 0$, then $f_{\rm mr} \approx 1$, and we end up with the thin-target approximation to determine the cross sections.

We can describe y_2 following Ref. [36] as

$$y_2(r) \approx \frac{1}{2}\sum_{r2} \mu N_b \sigma(r)\mu\sigma(r_2 \to r) \times \exp\left[-\left(\sigma_b^T + \sigma_r^T + \sigma_{r2}^T\right)\mu/3\right]. \qquad (4)$$

This equation contemplates no other approximations than those described previously. Here, $\sigma(r_2 \to r)$ describes the production cross section of the residue r, as the result of the reaction of a previously formed nuclide r_2 within the target. All possible attenuations are already included in the σ^T terms. This description is valid assuming that the transmission of all nuclides is near 100%, which is our case. Otherwise, transmission coefficients should be included. The method relies on a realistic evaluation of the intermediate cross sections $\sigma(r2 \to r)$. We have evaluated those cross sections using an intranuclear cascade code, where the number and type of ejected nucleons, along with the associated excitation energy induced, were modeled phenomenologically. That code was coupled to the evaporation-fission code ABLA [35]. Our model proved to produce realistic results when compared with the isotopic distributions of our data and with existing data from other reactions such as ^{238}U(1A GeV)+p [8], ^{208}Pb(1A GeV)+p [3], and ^{208}Pb(1A GeV)+d [4].

The final value of $f_{\rm mr}$ was obtained by iteration. An initial value for $\sigma \approx \sigma_0$ makes it possible to evaluate $y(\sigma_0)$ using Eqs. (3) and (4). The difference $\Delta_0 = y - y(\sigma_0)$ results in a new set of values $\sigma_1 = \sigma_0 + \Delta_0$. A new iteration using $\sigma \approx \sigma_1$ gives the difference $\Delta_1 = y - y(\sigma_1)$ and so on. The convergence of the method and the value $\sigma = \sigma_k$ is given for $y(\sigma_k) \approx y$ within the accuracy of our data.

In Fig. 8(d) we plot the correction factor $f_{\rm mr}$ as a function of the mass number of the residues. The line is the average value, weighted by each isobar production. The symbols represent $f_{\rm mr}$ for elements $_{65}$Tb, $_{75}$Re, and $_{85}$At. We can see that the correction corresponds to an almost constant 15% increase of the measured production, for the neutron-rich part of the isotopic distributions, corresponding to the attenuation of the nuclides passing through the target. The neutron-deficient side has a larger contribution due to multiple reactions, as is expected for evaporation residues. The resulting correction reduces the measured yields, in particular for the lightest residues.

The accuracy of this correction is determined by the accuracy of the evaluation of $\sigma(r2 \to r)$. To determine how that influences our results, the factor $f_{\rm mr}$ was reevaluated using values for $\sigma(r2 \to r)$ up to two times higher than the values provided by our codes. The difference between the two sets of $f_{\rm mr}$ values gives a limiting uncertainty, ranging from 1% for the heaviest residues to 50% for the lightest. A correction value of 50% was chosen as the upper limit: residues with larger corrections were not considered in this analysis.

C. Contributions from different reaction mechanisms

The reaction residues with atomic number above 60, typically neutron-deficient isotopes, are mainly produced by spallation-evaporation processes. However, asymmetric hot-fission channels can also contribute to the production of those nuclides, causing the two production sources to overlap. The two reaction mechanisms present different kinematic properties: spallation-evaporation residues have a longitudinal momentum p_L distribution with a Gaussian profile in the projectile frame, while the spallation-fission residues show a flat profile. The observed shape is also affected by the FRS acceptance. In our case, both spallation-evaporation and spallation-fission residues with atomic numbers above 60 have transmissions close to 100% [28], and the measured momentum distributions were not distorted.

In Fig. 10 we plot the measured p_L distributions of three neutron-rich nuclei: ^{205}At, ^{156}Dy, and ^{152}Sm, the region where we expect a transition between the mentioned reaction mechanisms. The Gaussian shape of ^{205}At is associated with spallation-evaporation processes, while the flat shape of ^{152}Sm is associated with spallation-fission. ^{156}Dy represents

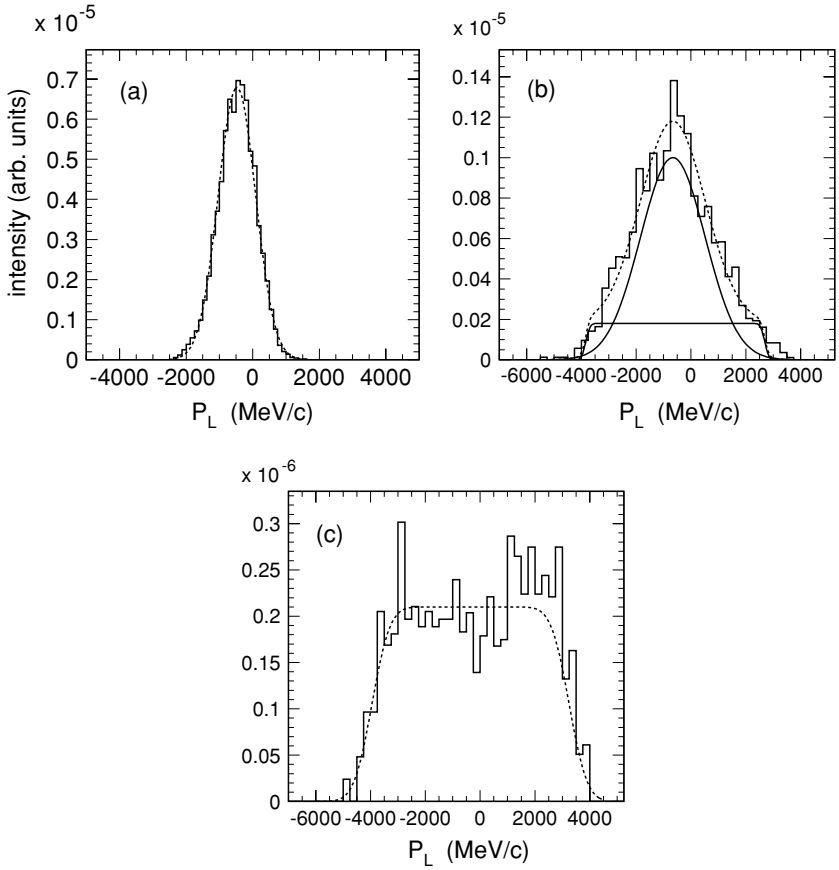

FIG. 10. Measured longitudinal momentum distribution in the projectile frame for (a) $^{205}_{85}$At, (b) $^{156}_{66}$Dy, and (c) $^{152}_{62}$Sm. The change of shape from a Gaussian to a flat distribution is associated with the different reaction mechanisms contributing to the production of the nuclides.

an intermediate case, where both mechanisms are present: a Gaussian shape added to a flat distribution. The systematics of our data show that for nuclides with Z above 70 the fission contribution seems to be negligible. The momentum distributions $f(p_L)$ of neutron-rich nuclides with Z below 70 were fitted to a combination of a Gaussian function representing the production by evaporation $f^{\text{evap}}(p_L)$, and a rectangular function folded with a Gaussian corresponding to fission $f^{\text{fiss}}(p_L)$, i.e. $f(p_L) = f^{\text{evap}}(p_L) + f^{\text{fiss}}(p_L)$, where

$$f^{\text{evap}}(p_L) = N^{\text{evap}} \exp\left[-\left(p_L - \langle p_L^{\text{evap}} \rangle\right)^2 / \left(\sqrt{2}\sigma_{p_L}^{\text{evap}}\right)^2 \right], \quad (5)$$

with $\langle p_L^{\text{evap}} \rangle$ and $\sigma_{p_L}^{\text{evap}}$ being the mean value and the width of the longitudinal momentum distribution due to the evaporation process. The function f^{fiss} is the folding of a Gaussian and a rectangular distribution

$$f^{\text{fiss}}(p_L) = 0.5 N^{\text{fiss}} \left[\text{erf}\left(\pi_L^+\right) - \text{erf}\left(\pi_L^-\right) \right], \quad (6)$$

where erf is the normalized error function, $\pi_L^{\pm} = (\langle p_L^{\text{fiss}} \rangle \pm \sigma_{p_L}^{\text{fiss}} - p_L)/\sqrt{2\sigma_o^2}$, $\langle p_L^{\text{fiss}} \rangle$ and $\sigma_{p_L}^{\text{fiss}}$ are the mean value and the variance of the longitudinal momentum distribution due to fission, and σ_o is the diffuseness of this rectangular distribution at the borders. The different parameters of these functions were constrained from the longitudinal momentum distributions for the most neutron-deficient and neutron-rich residues of each isotopic chain, where evaporation or fission are dominant, respectively. The ratio of the normalization factors N^{fiss} and N^{evap} determined the weight of the contribution from each process, $f_{\text{evap}} = N^{\text{evap}}/(N^{\text{evap}} + N^{\text{fiss}})$ in Eq. (1). In Fig. 10 we plot the result of the fit (dashed line) on top of some measured distributions. In the case of ^{156}Dy, the two components of the fit are also plotted separately (solid lines). The accuracy of the separation method used was estimated to be about 30%. Note that less than 10% of all measured isotopes, found to be produced by the two mechanisms, were affected by this correction.

D. Uncertainties

The accuracy of the isotopic production cross sections was determined from the uncertainties of the production yields $y(r)$, beam intensity N_b, and target thickness μ. The uncertainty in beam intensity was estimated to be around 4% [22]. The uncertainty in the target thickness was evaluated accounting for the deformation of the target walls, and the alignment of both the target axis and the beam axis. Both effects were investigated with a specially designed measurement [37]. Our evaluation of the combined effects shows that the target thickness variation was less than 1% for 80% of the projectiles, and less than 3% for the total distribution. The influence of tiny temperature fluctuations on the density of the target during the experiment was negligible.

The accuracy of the yield $y(r)$ was determined by the uncertainties of the correction factors applied (f_τ, f_Q, f_{loss}, f_{acc}, y_{tar}, and f_{evap}) and the statistical uncer-

tainty. The statistical uncertainty $\sqrt{N}$ for a given number of measured events N, remained below 10% for most of the nuclides, corresponding to production cross sections down to 10 μb. An additional test of statistical accuracy was done by comparing the measured cross sections of nuclides along paths in the chart of nuclides with a softer change than that of the isotopic chains [3]. We have used the chains having an $(N - Z)$ or $(N - 2Z)$ constant. Since even-odd or shell effects are not observed, the deviations observed in the measured productions from the smoothed trend can be used as a test of the statistical uncertainty. We found that all deviations in these tests were within the statistical uncertainties.

The uncertainties of the measured production cross sections were less than 6% statistical and less than 15% systematic for 85% of the data, for the charge range covered by this experiment ($Z = 92$ to $Z = 58$). For some isotopes of elements with Z below 70, an additional systematic uncertainty (f_{evap}) accounts for the separation between fragmentation and fission production. The most neutron-deficient isotopes can also show larger uncertainties due to the contribution of multiple reactions.

IV. RESULTS AND DISCUSSION

Figures 11 and 12 show the isotopic distributions of the measured production cross sections corresponding to the 602 nuclei identified as evaporation residues in the reaction ^{238}U(1A GeV)+d. All values are tabulated in the Appendix.

A few residues (^{234}Pa, ^{231,232}Th, $^{229-231}$Ac, ^{226,227}Ra, $^{223-227}$Fr) could not be measured because their magnetic rigidities were too close to that of the beam. Other nuclides, corresponding to the neutron-rich side of the lightest elements (Pm, Nd, Pr, Ce), could not be accurately separated in both evaporation and fission components and were discarded in our analysis. Additionally, the cross sections of some isotones with $N = 128$ were not correctly measured because of their very fast α decay. The half-lives of these nuclides are shorter than their time of flight through the FRS (≈150 ns, proper time), and they partially decayed in flight, leading to a depopulation of the observed production of residues with $N = 128$, and an overestimation of the production of nuclides with $N = 126$. The isotones $N = 127$ are also affected by misidentifications. To correct all of these effects would decrease the accuracy, because of both the uncertainty associated with the half-lives of the nuclides involved and the presence of isomers with unknown branching ratios. The amount, quality, and smooth trend of our data allows for an accurate evaluation of the values of those particular cases with an adequate interpolation. The total cross section amounts to 908 mb (747 mb measured plus 161 mb estimated to be missing), with uncertainties of 13 mb (statistical) and 111 mb (systematic).

The analysis of the shape of the isotopic distributions, Figs. 11 and 12, reveals the influence of the different reaction mechanisms involved in the production of the isotopes. In general, the spallation-evaporation residues are neutron-deficient nuclides, with the maximum of production around a position determined by the equilibrium in the competition between proton and neutron emission. Close to the projectile, the distributions are wider. This is due to the difference in neutron excess between the projectile and the above mentioned equilibrium position. Lighter residues, produced by longer evaporation chains, show a uniform behavior: they become similar in width and the maximum production is defined by the equilibrium position. We also note that the production of neutron-deficient residues of heavier elements drops drastically following the evolution of the fission barriers. As expected, the production of highly fissile residues is strongly suppressed.

It is important to note that the data do not show odd-even effects, which have been observed for light residues [38]. A similar effect was noted in the data obtained for the reaction ^{208}Pb(1A GeV)+d [4]. The washing out of even-odd effects for heavy residues is attributed to the increased probability of deexcitation by γ emission with a higher mass number. It is also worth noting that no enhancing effects in production appear around $N = 126$. As demonstrated in [39], collective effects in level densities associated with the saddle point and the ground-state configurations counteract the enhancement of production around the shell closures. Therefore, structural effects are hindered even at low excitation energies.

In Fig. 13, we plot the same production cross sections distributed as a function of the mass and atomic numbers. The large effect of fission in the production of residual nuclei is notable in mass numbers above 190 and atomic numbers above 80.

In Fig. 14, we show a scatter plot of the measured production cross sections on top of a chart of nuclides. The maximum of the production forms a line along the neutron-deficient side of the β-stability valley, which is determined by the equilibrium between proton and neutron emissions. This equilibrium position is known as the "evaporation corridor" [40] and is similar for all systems reaching the limiting fragmentation regime [41]. Our data follow the evaporation corridor for Z values below 82. Heavier residues form a different slope in the maximum isotopic production, moving from the corridor to the nuclides that are closer to the projectile. This effect is due to two factors: the limited excitation energy induced in the most peripheral collisions, which results in residues with enhanced neutron emission in the neighborhood of the projectile; and the influence of the fission mechanism, which strongly depletes the production of neutron-deficient residues.

The limiting fragmentation concept can also be investigated in Fig. 15, where we represent the N/Z ratio of the observed residual nuclei as a function of their mass number. The N/Z values shown in this figure are averaged over isobaric chains and weighted by the production cross section of each residue. The solid line represents the prediction of the (EPAX) formula [42], based on the limiting fragmentation hypothesis. The heavier residues observed in this work are more neutron-rich than those predicted by EPAX, because EPAX was not formulated to describe reactions where the fission mechanism is present and dominant, as in our case. We do not observe any noticeable deviations indicating an excess of neutrons for lighter residues, as stated in Ref. [43]. In that work, the authors observed a clear deviation with respect

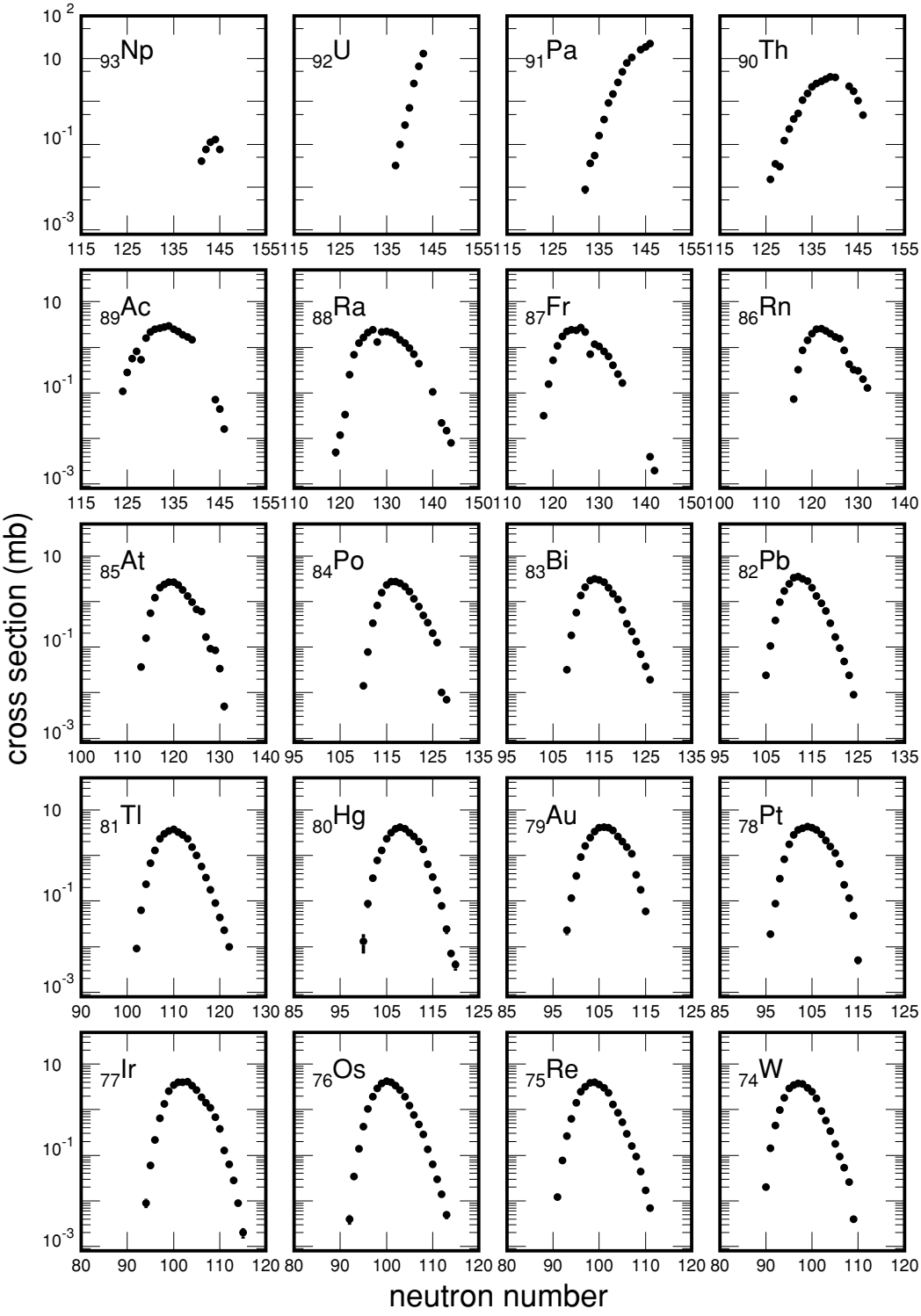

FIG. 11. Isotopic cross sections of residual nuclei $_{93}$Np to $_{74}$W produced in reactions induced by ^{238}U(1A GeV) with deuterium. Error bars for statistical uncertainty, are visible only when larger than the symbol size.

to the evaporation corridor, with larger neutron excesses in light residues produced in reactions induced in ^{238}U(1A GeV) with titanium and lead targets. That deviation was interpreted as a signature of multifragmentation. The fact that we do not observe those deviations with respect to the evaporation corridor seems to indicate that the excitation energy induced by the deuterons is not sufficient to reach the multifragmentation regime.

Another remarkable result is the observation of fission residues with Z from 58 to 69, indicating extremely asymmetric hot fission processes. These results are explored in detail in Ref. [1].

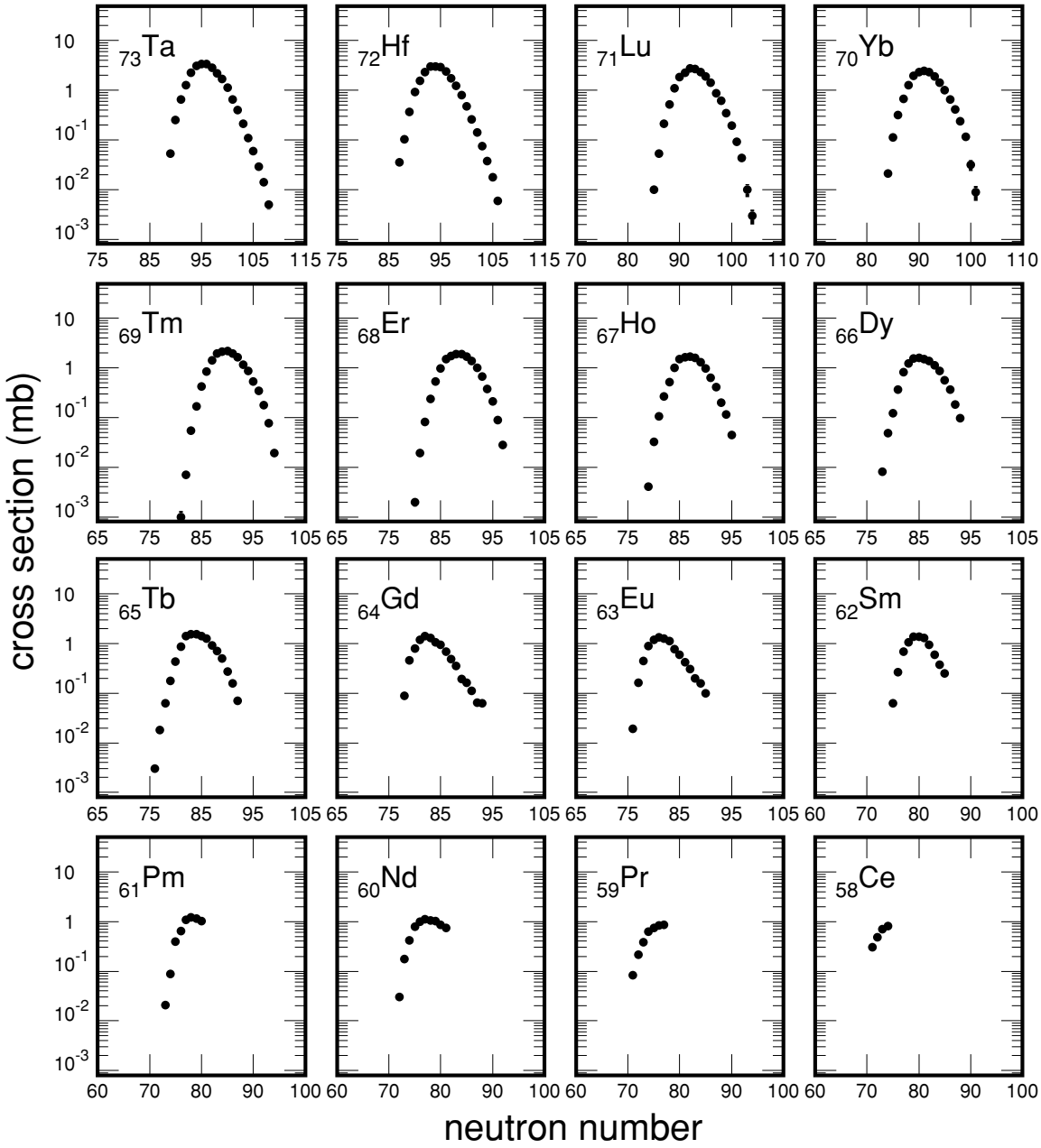

FIG. 12. Same as Fig. 11, but for residual nuclei $_{73}$Ta to $_{58}$Ce.

A. Comparison to other data

The systematic investigation of the residue production in fragmentation and spallation reactions performed during the last years has produced a large high-quality set of data [2–12] that can help us appreciate the most salient features of the system investigated in this work.

In Fig. 16, we compare the isotopic distributions of residual nuclides produced in the reactions ^{238}U(1A GeV)+p [8] and ^{238}U(1A GeV)+d for several elements. Here, we observe that the production cross sections of heavy residues are rather similar in both reactions. However, the production of lighter residues decreases faster for reactions induced by protons than for those induced by deuterons. Both observations can be understood by looking at the first stage of the collision. Heaviest residual nuclei are produced in very peripheral collisions, where ^{238}U hits only one of the two deuterium nucleons. This effect is enhanced by the wide spatial distribution of deuterons. Under such conditions, reactions induced by protons and deuterons would be similar. At smaller impact parameters, ^{238}U interacts with both deuterium nucleons, inducing on the average up to twice the excitation energy when compared with proton collisions. Higher excitation energy leads to longer evaporation chains in the case of deuteron-induced reactions, thus populating more the lighter residues.

The large amount of measured data also allows for an accurate reconstruction of the isobaric distribution of the

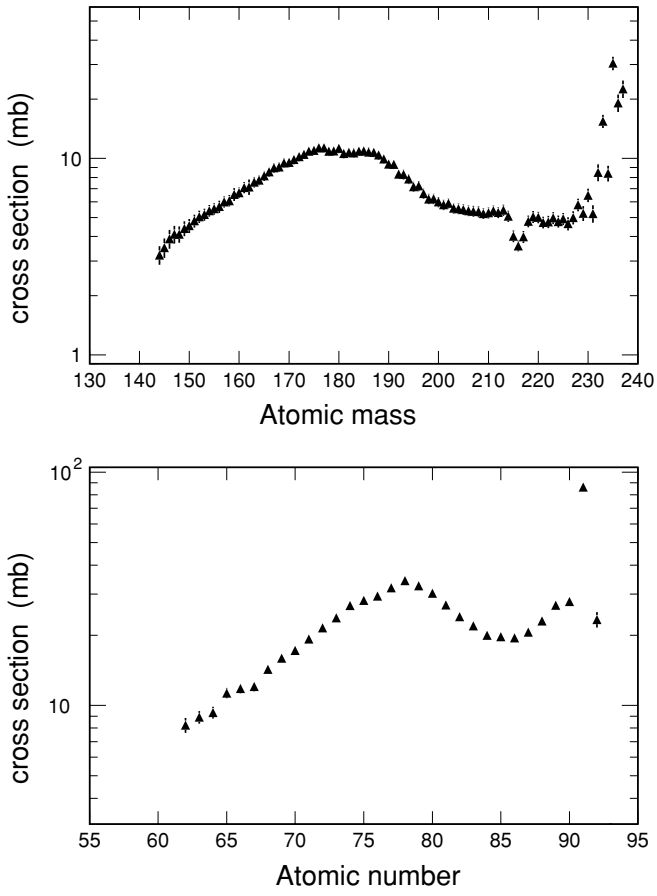

FIG. 13. Production cross sections of the residues measured in the reaction ^{238}U(1A GeV)+d plotted as function of the residue mass number and atomic number. Total error bars are visible only if larger than the symbols.

production cross section. In Fig. 17, we show the isobaric distribution of residues produced in the reactions ^{208}Pb(1A GeV)+d [4], ^{238}U(1A GeV)+p [8], and ^{238}U(1A GeV)+d. The isobaric distributions of residual nuclides produced in reactions of ^{208}Pb and ^{238}U with deuterium present a very different pattern. In reactions of ^{238}U induced by deuterons,

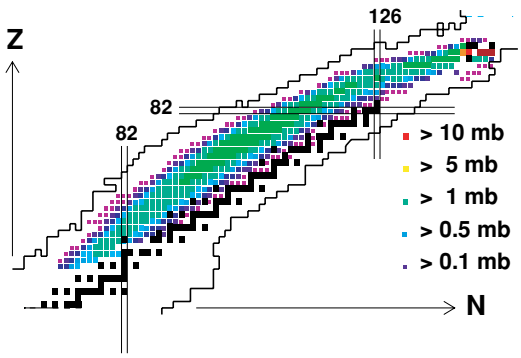

FIG. 14. (Color online) Production cross sections of residues measured in the reaction ^{238}U(1A GeV) on deuteron plotted in gray scale (color scale in the online edition) on top of a chart of nuclides. Black boxes are stable nuclides.

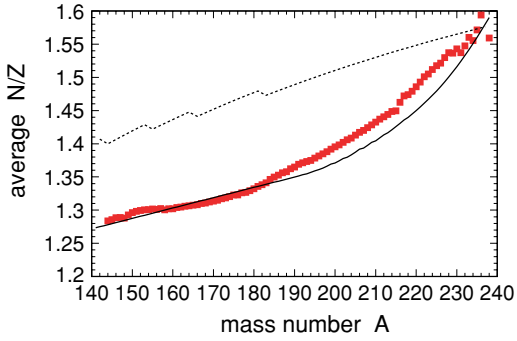

FIG. 15. (Color online) Average N/Z ratio of the residual nuclei measured work as a function of their mass number. Solid line represents the prediction of the EPAX formula [42]. Dashed line is the stability line.

the evaporation cross section, 908 mb, represents about 36% of the total reaction cross section value predicted by Glauber-type calculations [30,31]. However, for the Pb+d data, the measured evaporation residues represent about 90% of the total reaction cross section. Other residual distributions, such as those of ^{208}Pb(1A GeV)+p [3] and ^{197}Au(850A MeV)+p [6], not shown here, produce similar isobaric profiles, but scaled by the ratio of the total reaction cross sections. The observed difference between ^{208}Pb and ^{238}U is clearly due to the strength of the fission channel, which largely dominates the reaction in the neighborhood of ^{238}U. Fission actually depopulates the heavier residues and populates medium-mass residues, which appear beyond the lower mass limit of Fig. 17, see Ref. [1].

The isotopic distributions shown in Figs. 11 and 12 reveal that the observed depopulation due to fission affects especially to neutron-deficient residues, following the evolution of the fission barriers. Consequently, we can conclude that the production of neutron-deficient heavy residues in the region of Z higher than 80 requires high beam intensities to efficiently reach the proton drip line. This effect will cause severe difficulties for the production of heavy proton-emitter candidates.

We also observe in Fig. 17 that in spite of the role of fission in the production of residues in reactions induced in ^{238}U, the production of light evaporation residues ($\Delta A > 70$) is very similar to that obtained from ^{208}Pb, where fission plays a minor role. This observation is interpreted as a signature of the role of nuclear matter viscosity, which suppresses fission at high excitation energy, thus enhancing the production of lighter evaporation residues. This topic is discussed at length in Ref. [44].

B. Recoil longitudinal momentum and kinetic energy

The energy transferred in the reaction mechanism leading to the production of a given nuclide includes both a momentum shift and a broadening. The experimental method used in this work allows for both the identification and determination of production cross sections of the projectile residual nuclei and the measurement of their longitudinal momentum distribution. In the case of evaporation residues, the observed momenta distributions are Gaussian-like, see Fig. 7. This shape results

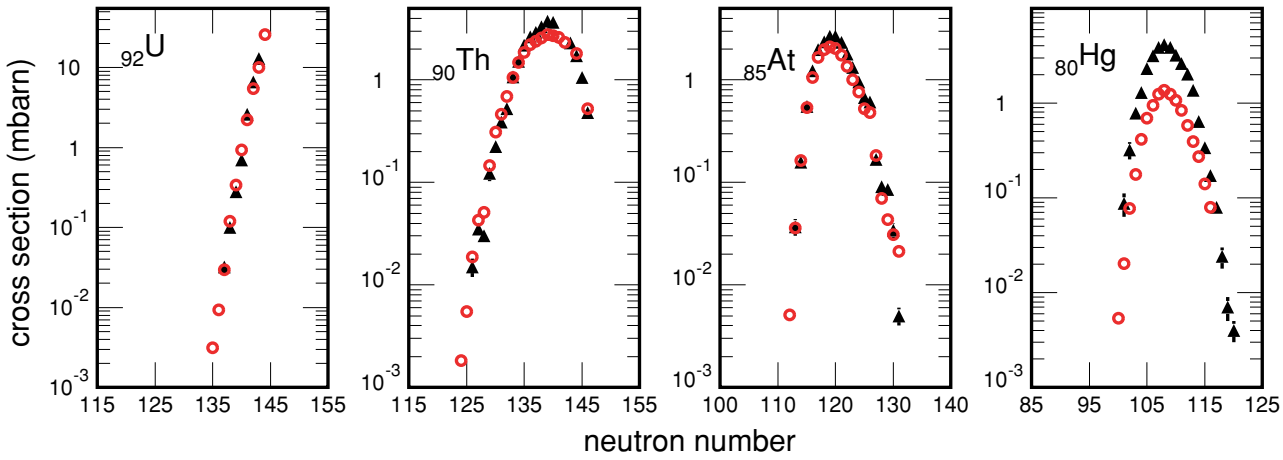

FIG. 16. (Color online) Isotopic cross sections of residual nuclides of $_{92}$U, $_{90}$Th, $_{85}$At, and $_{80}$Hg, produced in reactions of ^{238}U(1A GeV)+d (triangles) and ^{238}U(1A GeV)+p [8] (circles).

from the combination of different processes. In addition to the reaction itself, atomic interactions in the target, such as energy straggling, location straggling, and beam spread, contribute to the observed distribution. In order to determine the momentum shift and broadening that characterize the reaction mechanism, the measured distributions must be unfolded from the mentioned effects. The broadening due to the energy spread of the beam and its straggling in the target follows Gaussian-like distributions. This width can be determined experimentally from the measured momentum distribution of the primary beam behind the target. In our case we obtained a width of 118 MeV/c (FWHM). Location straggling, due to the spread associated with the different reaction points along the target thickness, follows a rectangular distribution that can be evaluated from accurate energy-loss calculations [45].

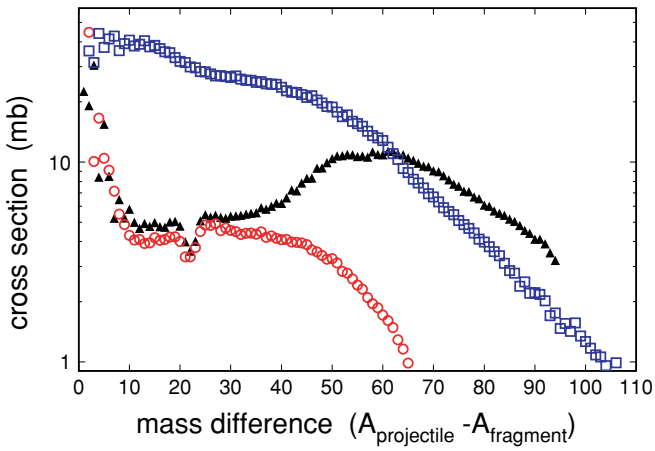

FIG. 17. (Color online) Isobaric distribution of production of evaporation residues in the reactions induced by ^{208}Pb (1A GeV)+d [4] (squares), ^{238}U(1A GeV)+p (circles) [8], and ^{238}U(1A GeV)+d (triangles). These distributions are represented as a function of the difference in residue mass with respect to the projectile. Only statistical error bars are shown (visible if larger than the symbols).

In Fig. 18, we plotted the average momentum $\langle p_L \rangle$ and width of those distributions σ_{p_L} as a function of the mass difference ΔA between the projectile and the residues, in the frame defined by the projectile velocity at the middle of the target. The accuracy in the measurement of the position of each fragment at the intermediate focal plane of the FRS (3 mm) determines the accuracy for momentum, typically 84 MeV/c for ^{238}U, and 54 MeV/c for ^{150}Tb. The values are averaged for each isobaric chain and weighted by the measured cross sections. The comparison of the results with the values given by the Morrissey systematics [46] reveals that the measured data follow the systematic trend for both averaged momentum and width, up to mass differences of 60 units. For $\Delta A > 60$ the average momentum saturates, while the width increases considerably. These two effects cannot be explained as fission contamination in our distributions. Moreover, a similar trend is observed in the residues of the reaction ^{208}Pb(1A GeV)+d [4], where fission is not involved. This effect has also been observed clearly in heavy-ion collisions, where it has been attributed to the influence of the participant blast to the momentum of the projectile spectator, as discussed in detail in Ref. [47].

In Fig. 18(b), the unfolded widths are also compared with the predictions of the Goldhaber model [48]. This model considers the width of the momentum distribution to be entirely due to the Fermi momentum of the nucleons abraded during the first stage of the reaction. Subsequent deexcitation effects are not considered. Therefore, residues resulting from very peripheral collisions, where very low excitation energy is induced, should follow the Goldhaber mechanism, since these residues do not undergo further deexcitation processes [49]. We found that the one-, two-, and three-proton removal channels do indeed have a momentum width definitely closer to the Goldhaber prediction, as can be seen in the insert of Fig. 18(b).

We can also define the recoil kinetic energy T from the measured momenta distributions as

$$T = \tfrac{1}{2} Au\left(\langle \beta_L \rangle^2 + 3\left(\sigma_{\beta_L}\right)^2\right), \tag{7}$$

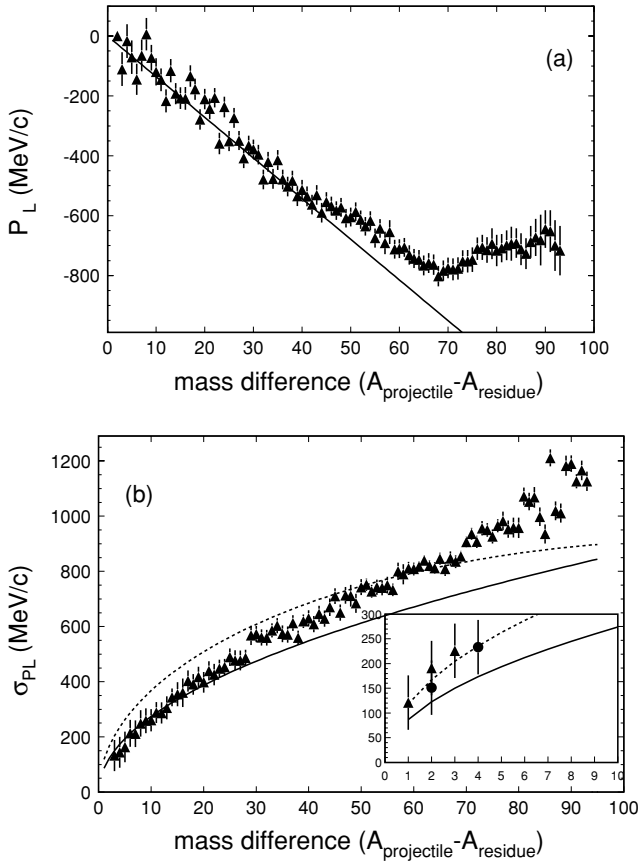

FIG. 18. (a) Measured longitudinal momentum $\langle p_L \rangle$ plotted as function of mass difference $\Delta A = A_{\text{projectile}} - A_{\text{residue}}$. Line corresponds to the Morrissey systematics [46]. (b) Unfolded width σ_L of the $\langle p_L \rangle$ distribution plotted as function of ΔA. Lines correspond to the Morrissey systematics [46] (solid line) and the Goldhaber model [48] (dashed line). Insert shows data of the one-, two-, and three-proton removal channels (triangles) and one additional neutron removal (circles).

where A is the mass number and u the atomic mass unit. Velocity β_L and momentum p_L are directly related inside the projectile frame. The factor 3 accounts for the fact that we measure the projection of the three-dimensional distribution into the longitudinal component, p_L. The values for T were obtained from the averaged values $\langle p_L \rangle$ and σ_{p_L}; they are plotted in Fig. 19 as a function of ΔA and compared to the Morrissey systematics.

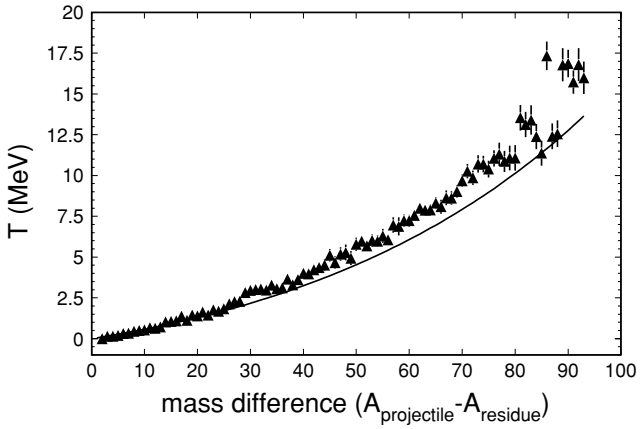

FIG. 19. Recoil kinetic energy T obtained after the measured values of $\langle p_L \rangle$ and σ_L, as function of mass difference $A_{\text{projectile}} - A_{\text{residue}}$. Solid line is the value given by the Morrissey systematics [46].

V. CONCLUSIONS

In this work, we have investigated the production of residual nuclei in spallation reactions of ^{238}U(1A GeV) with deuterium. We have identified 602 residues, with Z ranging from 93 to 58 and with production cross sections above 2 μb. The production cross sections of all these residues give a total evaporation cross section of 908±13±111 mb. The statistical quality of our data is very high, and the systematic uncertainties are low. Unambiguous identification and determination of the production cross sections of heavy residues is a well-recognized challenge, requiring a great deal of experimental effort, an especially designed high-performance setup, and a proper identification method. The inverse kinematics technique made possible the unambiguous identification of all the primary production of projectile residues in the reaction under study, as well as the measurement of their longitudinal momentum. Additionally, kinematic signatures allowed us to disentangle the reaction mechanisms responsible for the production of the measured residues, namely evaporation and fission.

The width and position of the maximum production of the isotopic distributions change from wide distributions centered around neutron-rich nuclei close to the projectile, to narrower distributions of similar width centered on the neutron-deficient side, along the so-called evaporation corridor. The homogeneous shape of the isotopic distributions along this corridor are an indication of the limiting fragmentation regime reached at high excitation energies and leading to longer evaporation chains.

The production of heavy residues clearly shows the effects of fission, notably the depopulation of neutron-deficient residues due to their higher fissility. We also note the absence of odd-even effects in the isotopic distributions of heavy residues as well as the absence of an enhanced production of residues around the closed neutron shell $N = 126$. In our data, we do not observe deviations from the evaporation corridor for the lighter residues, observed in other works using similar reactions but induced by heavier targets. These deviations have been understood as a possible signature of multifragmentation that we apparently do not reach in our system.

When compared to other reactions, our data reveal some interesting features. The comparison of the production of residual nuclei in reactions induced by protons and deuterium on ^{238}U show the influence of the larger excitation energy available in the system for the deuterium case. Higher excitation energies lead to longer deexcitation chains that populate lighter nuclides, extending the fragmentation production to masses about 100 units lighter than that of the projectile. Additionally, peripheral reactions induced by deuterium enhance the probability of single-nucleon collisions, due in part to the wide matter distribution of the deuterium. In fact, proton- and

deuteron-induced reactions show similar isotopic distributions of heavy residual nuclei. This observation confirms that there is no difference between proton- and neutron-induced collisions at these energies. Since the deuteron is the simplest extension after the collision of a single nucleon, this comparison of proton- and deuteron-induced reactions will also make it possible to improve the description of reactions induced by heavier targets.

The possibility of reconstructing the isobaric distribution of residual nuclei helps to reveal the influence of fission. This is especially noticeable in the comparison of residue production in deuteron-induced reactions in ^{208}Pb and ^{238}U, which shows a clear depopulation in the latter case due to the higher fissility of the nuclei produced. This depopulation of evaporation residues due to fission has been used as a signature of fission dynamics at high excitation energy.

The importance of model calculations describing spallation processes is well-recognized in applications such as the production of radioactive nuclear beams, design of neutron sources, or interpretation of cosmic-ray abundances. These applications require model calculations with a high predictive power that has not been attained by existing codes. The data presented in this work provide an excellent database for constraining and improving those models.

ACKNOWLEDGMENTS

We wish to thank K. H. Behr, A. Brünle, and K. Burkard for their technical support during the experiment, as well as the group of P. Chesny, who built the liquid-hydrogen target. This work was partially supported by the Spanish Ministry of Education and Science and Xunta de Galicia under Contracts FPA2002-04181-C04-01 and PGIDT01PXI20603PM, respectively, and the European Community under the contracts "Access to Research Infrastructure Action of the Improving Human Potential" PRI-CT-1999-00001, "HINDAS" FIKW-CT-2000-00031 and "Research Infrastructure Action—Structuring the European Research Area" EURISOL DS Project Contract No. 515768 RIDS.

APPENDIX: MEASURED CROSS SECTIONS

TABLE I. Isotopic cross sections of spallation-evaporation residues of ^{238}U(1A GeV)+d, with statistical and systematic uncertainties.

Nucleus	σ (mb)	ε_{STAT} (mb)	ε_{SYST} (mb)	nucleus	σ (mb)	ε_{STAT} (mb)	ε_{SYST} (mb)
^{234}Np	0.041	0.005	0.004	^{237}Pa	22.464	0.182	2.316
^{235}Np	0.076	0.006	0.008	^{216}Th	0.015	0.002	0.002
^{236}Np	0.112	0.007	0.012	^{217}Th	0.035	0.004	0.003
^{237}Np	0.130	0.007	0.013	^{218}Th	0.030	0.002	0.003
^{238}Np	0.076	0.006	0.008	^{219}Th	0.122	0.015	0.012
^{229}U	0.032	0.004	0.004	^{220}Th	0.225	0.008	0.022
^{230}U	0.100	0.007	0.012	^{221}Th	0.390	0.011	0.040
^{231}U	0.279	0.014	0.034	^{222}Th	0.522	0.011	0.054
^{232}U	0.699	0.024	0.085	^{223}Th	1.071	0.014	0.112
^{233}U	2.619	0.046	0.311	^{224}Th	1.517	0.024	0.160
^{234}U	6.593	0.095	0.748	^{225}Th	2.183	0.034	0.231
^{235}U	13.040	0.124	1.601	^{226}Th	2.625	0.039	0.283
^{223}Pa	0.009	0.002	0.001	^{227}Th	2.915	0.038	0.326
^{224}Pa	0.036	0.004	0.004	^{228}Th	3.300	0.041	0.374
^{225}Pa	0.054	0.003	0.008	^{229}Th	3.755	0.066	0.420
^{226}Pa	0.160	0.006	0.020	^{230}Th	3.626	0.049	0.405
^{227}Pa	0.376	0.014	0.046	^{233}Th	2.285	0.013	0.250
^{228}Pa	0.926	0.023	0.104	^{234}Th	1.728	0.011	0.188
^{229}Pa	1.470	0.031	0.168	^{235}Th	1.055	0.009	0.115
^{230}Pa	2.753	0.038	0.304	^{236}Th	0.478	0.005	0.052
^{231}Pa	4.944	0.083	0.529	^{213}Ac	0.109	0.005	0.011
^{232}Pa	7.778	0.081	0.822	^{214}Ac	0.280	0.008	0.027
^{233}Pa	10.472	0.107	1.111	^{215}Ac	0.557	0.012	0.054
^{235}Pa	16.321	0.501	1.712	^{216}Ac	0.808	0.020	0.079
^{236}Pa	18.610	0.165	1.945	^{217}Ac	0.539	0.009	0.055

TABLE II. Isotopic cross sections of spallation-evaporation residues of ^{238}U(1A GeV)+d, with their statistical and systematic uncertainties.

Nucleus	σ (mb)	ε_{STAT} (mb)	ε_{SYST} (mb)	Nucleus	σ (mb)	ε_{STAT} (mb)	ε_{SYST} (mb)
^{218}Ac	1.599	0.020	0.159	^{218}Ra	2.229	0.106	0.250
^{219}Ac	2.169	0.102	0.219	^{219}Ra	2.111	0.050	0.235
^{220}Ac	2.519	0.037	0.257	^{220}Ra	1.860	0.038	0.208
^{221}Ac	2.603	0.045	0.271	^{221}Ra	1.472	0.026	0.167
^{222}Ac	2.825	0.033	0.302	^{222}Ra	1.247	0.021	0.140
^{223}Ac	2.923	0.041	0.315	^{223}Ra	0.973	0.020	0.110
^{224}Ac	2.508	0.034	0.279	^{224}Ra	0.713	0.022	0.081
^{225}Ac	2.251	0.028	0.251	^{225}Ra	0.437	0.016	0.050
^{226}Ac	1.874	0.030	0.210	^{228}Ra	0.105	0.003	0.012
^{227}Ac	1.700	0.029	0.186	^{230}Ra	0.022	0.001	0.003
^{228}Ac	1.474	0.021	0.158	^{231}Ra	0.015	0.001	0.002
^{233}Ac	0.071	0.002	0.009	^{232}Ra	0.008	0.001	0.001
^{234}Ac	0.044	0.002	0.005	^{205}Fr	0.032	0.003	0.003
^{235}Ac	0.016	0.001	0.002	^{206}Fr	0.157	0.006	0.016
^{207}Ra	0.005	0.001	0.001	^{207}Fr	0.513	0.012	0.051
^{208}Ra	0.012	0.002	0.001	^{208}Fr	1.080	0.018	0.107
^{209}Ra	0.033	0.003	0.003	^{209}Fr	1.731	0.021	0.171
^{210}Ra	0.249	0.009	0.024	^{210}Fr	2.233	0.031	0.226
^{211}Ra	0.696	0.012	0.068	^{211}Fr	2.431	0.028	0.251
^{212}Ra	1.228	0.016	0.120	^{212}Fr	2.348	0.044	0.253
^{213}Ra	1.660	0.024	0.164	^{213}Fr	2.732	0.024	0.292
^{214}Ra	2.105	0.027	0.210	^{214}Fr	2.189	0.022	0.242
^{215}Ra	2.402	0.041	0.243	^{215}Fr	0.705	0.012	0.086
^{216}Ra	1.296	0.017	0.149	^{216}Fr	1.156	0.015	0.141
^{217}Ra	2.169	0.022	0.238	^{217}Fr	1.048	0.032	0.126

TABLE III. Isotopic cross sections of spallation-evaporation residues of ^{238}U(1A GeV)+d, with their statistical and systematic uncertainties.

Nucleus	σ (mb)	ε_{STAT} (mb)	ε_{SYST} (mb)	Nucleus	σ (mb)	ε_{STAT} (mb)	ε_{SYST} (mb)
^{218}Fr	0.804	0.021	0.095	^{199}At	0.158	0.004	0.020
^{219}Fr	0.640	0.015	0.075	^{200}At	0.552	0.011	0.059
^{220}Fr	0.406	0.013	0.050	^{201}At	1.223	0.017	0.127
^{221}Fr	0.260	0.011	0.032	^{202}At	1.984	0.038	0.204
^{222}Fr	0.164	0.006	0.021	^{203}At	2.364	0.023	0.245
^{228}Fr	0.004	0.001	0.001	^{204}At	2.674	0.030	0.276
^{229}Fr	0.002	0.0003	0.0003	^{205}At	2.653	0.026	0.275
^{202}Rn	0.074	0.004	0.009	^{206}At	2.338	0.024	0.245
^{203}Rn	0.324	0.009	0.035	^{207}At	1.798	0.026	0.191
^{204}Rn	0.851	0.014	0.087	^{208}At	1.322	0.015	0.144
^{205}Rn	1.413	0.019	0.145	^{209}At	0.960	0.015	0.107
^{206}Rn	2.005	0.022	0.209	^{210}At	0.670	0.020	0.078
^{207}Rn	2.502	0.034	0.266	^{211}At	0.606	0.010	0.066
^{208}Rn	2.561	0.032	0.278	^{212}At	0.167	0.004	0.024
^{209}Rn	2.294	0.024	0.257	^{213}At	0.091	0.003	0.011
^{210}Rn	2.010	0.024	0.227	^{214}At	0.085	0.004	0.012
^{211}Rn	1.681	0.017	0.194	^{215}At	0.034	0.003	0.006
^{212}Rn	1.551	0.016	0.175	^{216}At	0.005	0.001	0.001
^{213}Rn	0.860	0.021	0.107	^{194}Po	0.014	0.001	0.006
^{214}Rn	0.426	0.006	0.052	^{195}Po	0.079	0.003	0.015
^{215}Rn	0.324	0.010	0.047	^{196}Po	0.332	0.006	0.042
^{216}Rn	0.307	0.010	0.038	^{197}Po	0.820	0.010	0.091
^{217}Rn	0.198	0.009	0.027	^{198}Po	1.547	0.018	0.161
^{218}Rn	0.128	0.010	0.017	^{199}Po	2.290	0.043	0.233
^{198}At	0.037	0.002	0.007	^{200}Po	2.743	0.025	0.276

TABLE IV. Isotopic cross sections of spallation-evaporation residues of ^{238}U(1A GeV)+d, with their statistical and systematic uncertainties.

Nucleus	σ (mb)	ε_{STAT} (mb)	ε_{SYST} (mb)	Nucleus	σ (mb)	ε_{STAT} (mb)	ε_{SYST} (mb)
^{201}Po	2.713	0.029	0.274	^{204}Bi	0.324	0.006	0.035
^{202}Po	2.540	0.029	0.255	^{205}Bi	0.221	0.004	0.024
^{203}Po	2.126	0.022	0.215	^{206}Bi	0.131	0.003	0.015
^{204}Po	1.651	0.026	0.167	^{207}Bi	0.069	0.002	0.008
^{205}Po	1.151	0.011	0.118	^{208}Bi	0.038	0.002	0.004
^{206}Po	0.782	0.013	0.081	^{209}Bi	0.019	0.001	0.002
^{207}Po	0.498	0.015	0.052	^{187}Pb	0.024	0.002	0.009
^{208}Po	0.341	0.008	0.036	^{188}Pb	0.106	0.004	0.024
^{209}Po	0.202	0.003	0.021	^{189}Pb	0.381	0.008	0.054
^{210}Po	0.126	0.003	0.013	^{190}Pb	0.978	0.016	0.111
^{211}Po	0.010	0.001	0.001	^{191}Pb	1.716	0.021	0.183
^{212}Po	0.007	0.001	0.001	^{192}Pb	2.439	0.025	0.252
^{191}Bi	0.032	0.002	0.013	^{193}Pb	3.306	0.043	0.336
^{192}Bi	0.180	0.005	0.032	^{194}Pb	3.504	0.032	0.354
^{193}Bi	0.576	0.012	0.071	^{195}Pb	3.154	0.033	0.320
^{194}Bi	1.340	0.019	0.143	^{196}Pb	2.839	0.029	0.287
^{195}Bi	2.060	0.024	0.212	^{197}Pb	2.010	0.024	0.207
^{196}Bi	2.901	0.044	0.292	^{198}Pb	1.333	0.028	0.141
^{197}Bi	3.152	0.031	0.316	^{199}Pb	0.910	0.023	0.097
^{198}Bi	2.954	0.033	0.296	^{200}Pb	0.623	0.008	0.067
^{199}Bi	2.692	0.029	0.270	^{201}Pb	0.330	0.006	0.037
^{200}Bi	1.988	0.024	0.201	^{202}Pb	0.165	0.003	0.021
^{201}Bi	1.493	0.022	0.152	^{203}Pb	0.096	0.002	0.012
^{202}Bi	1.129	0.020	0.115	^{204}Pb	0.049	0.002	0.006
^{203}Bi	0.658	0.009	0.068	^{205}Pb	0.024	0.001	0.004

TABLE V. Isotopic cross sections of spallation-evaporation residues of ^{238}U(1A GeV)+d, with their statistical and systematic uncertainties.

Nucleus	σ (mb)	ε_{STAT} (mb)	ε_{SYST} (mb)	Nucleus	σ (mb)	ε_{STAT} (mb)	ε_{SYST} (mb)
^{206}Pb	0.009	0.001	0.001	^{183}Hg	0.780	0.029	0.092
^{183}Tl	0.009	0.001	0.004	^{184}Hg	1.293	0.012	0.146
^{184}Tl	0.062	0.002	0.015	^{185}Hg	2.316	0.076	0.244
^{185}Tl	0.233	0.006	0.036	^{186}Hg	3.174	0.200	0.325
^{186}Tl	0.674	0.010	0.081	^{187}Hg	3.857	0.119	0.389
^{187}Tl	1.287	0.020	0.142	^{188}Hg	4.132	0.137	0.413
^{188}Tl	2.358	0.024	0.244	^{189}Hg	3.864	0.037	0.386
^{189}Tl	2.974	0.028	0.304	^{190}Hg	3.203	0.071	0.320
^{190}Tl	3.410	0.041	0.347	^{191}Hg	2.605	0.034	0.261
^{191}Tl	3.765	0.033	0.378	^{192}Hg	2.024	0.019	0.202
^{192}Tl	3.248	0.032	0.329	^{193}Hg	1.362	0.015	0.137
^{193}Tl	2.851	0.029	0.288	^{194}Hg	0.636	0.009	0.066
^{194}Tl	2.300	0.025	0.233	^{195}Hg	0.337	0.007	0.036
^{195}Tl	1.544	0.029	0.158	^{196}Hg	0.171	0.006	0.019
^{196}Tl	0.997	0.030	0.104	^{197}Hg	0.079	0.006	0.009
^{197}Tl	0.567	0.007	0.060	^{198}Hg	0.024	0.005	0.003
^{198}Tl	0.329	0.006	0.036	^{199}Hg	0.007	0.001	0.001
^{199}Tl	0.175	0.004	0.020	^{200}Hg	0.004	0.001	0.001
^{200}Tl	0.091	0.002	0.011	^{177}Au	0.023	0.005	0.004
^{201}Tl	0.044	0.002	0.006	^{178}Au	0.117	0.009	0.018
^{202}Tl	0.023	0.001	0.003	^{179}Au	0.352	0.021	0.046
^{203}Tl	0.010	0.001	0.001	^{180}Au	0.918	0.054	0.105
^{180}Hg	0.013	0.006	0.005	^{181}Au	1.609	0.034	0.175
^{181}Hg	0.087	0.017	0.017	^{182}Au	2.482	0.030	0.262
^{182}Hg	0.320	0.048	0.044	^{183}Au	3.393	0.089	0.348

TABLE VI. Isotopic cross sections of spallation-evaporation residues of ^{238}U(1A GeV)+d, with their statistical and systematic uncertainties.

Nucleus	σ (mb)	ε_{STAT} (mb)	ε_{SYST} (mb)	Nucleus	σ (mb)	ε_{STAT} (mb)	ε_{SYST} (mb)
^{184}Au	4.104	0.126	0.415	^{188}Pt	1.120	0.014	0.112
^{185}Au	4.191	0.121	0.422	^{189}Pt	0.668	0.012	0.067
^{186}Au	4.041	0.090	0.405	^{190}Pt	0.225	0.005	0.024
^{187}Au	3.567	0.038	0.356	^{191}Pt	0.115	0.003	0.013
^{188}Au	2.570	0.069	0.259	^{192}Pt	0.048	0.002	0.006
^{189}Au	1.995	0.032	0.200	^{193}Pt	0.005	0.001	0.001
^{190}Au	1.516	0.017	0.151	^{171}Ir	0.009	0.002	0.002
^{191}Au	1.095	0.014	0.109	^{172}Ir	0.059	0.003	0.009
^{192}Au	0.380	0.006	0.041	^{173}Ir	0.218	0.007	0.032
^{193}Au	0.177	0.005	0.020	^{174}Ir	0.654	0.030	0.082
^{194}Au	0.059	0.003	0.008	^{175}Ir	1.343	0.067	0.156
^{174}Pt	0.019	0.003	0.003	^{176}Ir	2.543	0.061	0.272
^{175}Pt	0.087	0.006	0.014	^{177}Ir	3.453	0.044	0.362
^{176}Pt	0.314	0.011	0.042	^{178}Ir	3.967	0.042	0.411
^{177}Pt	0.826	0.024	0.098	^{179}Ir	3.949	0.051	0.407
^{178}Pt	1.749	0.059	0.189	^{180}Ir	4.061	0.094	0.415
^{179}Pt	2.851	0.044	0.297	^{181}Ir	3.397	0.112	0.348
^{180}Pt	3.679	0.041	0.377	^{182}Ir	2.662	0.028	0.272
^{181}Pt	3.925	0.053	0.402	^{183}Ir	1.876	0.022	0.194
^{182}Pt	4.313	0.136	0.435	^{184}Ir	1.415	0.016	0.146
^{183}Pt	4.048	0.126	0.407	^{185}Ir	1.099	0.026	0.111
^{184}Pt	3.677	0.033	0.367	^{186}Ir	0.689	0.026	0.070
^{185}Pt	2.930	0.036	0.293	^{187}Ir	0.380	0.007	0.039
^{186}Pt	2.134	0.070	0.214	^{188}Ir	0.129	0.004	0.014
^{187}Pt	1.571	0.033	0.157	^{189}Ir	0.063	0.002	0.007

TABLE VII. Isotopic cross sections of spallation-evaporation residues of ^{238}U(1A GeV)+d, with their statistical and systematic uncertainties.

Nucleus	σ (mb)	ε_{STAT} (mb)	ε_{SYST} (mb)	Nucleus	σ (mb)	ε_{STAT} (mb)	ε_{SYST} (mb)
^{190}Ir	0.028	0.002	0.003	^{166}Re	0.012	0.001	0.002
^{191}Ir	0.009	0.001	0.001	^{167}Re	0.076	0.003	0.012
^{192}Ir	0.002	0.001	0.0003	^{168}Re	0.266	0.006	0.041
^{168}Os	0.004	0.001	0.001	^{169}Re	0.635	0.007	0.093
^{169}Os	0.034	0.003	0.005	^{170}Re	1.435	0.036	0.179
^{170}Os	0.140	0.004	0.021	^{171}Re	2.457	0.018	0.277
^{171}Os	0.420	0.006	0.060	^{172}Re	3.202	0.053	0.349
^{172}Os	1.041	0.032	0.129	^{173}Re	3.919	0.041	0.409
^{173}Os	1.925	0.041	0.219	^{174}Re	4.041	0.064	0.416
^{174}Os	2.894	0.048	0.312	^{175}Re	3.552	0.047	0.363
^{175}Os	3.781	0.054	0.395	^{176}Re	3.022	0.052	0.308
^{176}Os	4.251	0.043	0.434	^{177}Re	2.324	0.057	0.236
^{177}Os	3.972	0.050	0.405	^{178}Re	1.309	0.015	0.137
^{178}Os	3.340	0.091	0.340	^{179}Re	0.857	0.013	0.090
^{179}Os	2.695	0.106	0.275	^{180}Re	0.535	0.009	0.056
^{180}Os	1.938	0.021	0.197	^{181}Re	0.297	0.007	0.031
^{181}Os	1.224	0.017	0.126	^{182}Re	0.158	0.004	0.017
^{182}Os	0.773	0.011	0.080	^{183}Re	0.094	0.003	0.010
^{183}Os	0.471	0.009	0.049	^{184}Re	0.044	0.002	0.005
^{184}Os	0.288	0.010	0.030	^{185}Re	0.017	0.001	0.002
^{185}Os	0.135	0.004	0.014	^{186}Re	0.007	0.001	0.001
^{186}Os	0.064	0.003	0.007	^{164}W	0.020	0.001	0.005
^{187}Os	0.030	0.002	0.004	^{165}W	0.141	0.005	0.075
^{188}Os	0.014	0.001	0.002	^{166}W	0.455	0.007	0.070
^{189}Os	0.005	0.001	0.001	^{167}W	0.980	0.010	0.138

TABLE VIII. Isotopic cross sections of spallation-evaporation residues of ^{238}U(1A GeV)+d, with their statistical and systematic uncertainties.

Nucleus	σ (mb)	ε_{STAT} (mb)	ε_{SYST} (mb)	Nucleus	σ (mb)	ε_{STAT} (mb)	ε_{SYST} (mb)
^{168}W	1.843	0.020	0.226	^{171}Ta	2.176	0.021	0.224
^{169}W	2.952	0.025	0.327	^{172}Ta	1.684	0.016	0.171
^{170}W	3.483	0.048	0.372	^{173}Ta	1.139	0.032	0.116
^{171}W	3.798	0.039	0.393	^{174}Ta	0.650	0.008	0.067
^{172}W	3.667	0.041	0.373	^{175}Ta	0.397	0.006	0.040
^{173}W	2.995	0.029	0.303	^{176}Ta	0.211	0.005	0.022
^{174}W	2.482	0.021	0.248	^{177}Ta	0.110	0.005	0.011
^{175}W	1.767	0.038	0.176	^{178}Ta	0.059	0.003	0.006
^{176}W	0.929	0.011	0.096	^{179}Ta	0.029	0.001	0.015
^{177}W	0.586	0.008	0.060	^{180}Ta	0.014	0.001	0.002
^{178}W	0.340	0.006	0.035	^{181}Ta	0.005	0.001	0.001
^{179}W	0.178	0.006	0.018	^{159}Hf	0.036	0.002	0.019
^{180}W	0.093	0.004	0.010	^{160}Hf	0.104	0.003	0.058
^{181}W	0.053	0.002	0.028	^{161}Hf	0.372	0.007	0.202
^{182}W	0.026	0.001	0.013	^{162}Hf	0.932	0.011	0.495
^{183}W	0.004	0.001	0.001	^{163}Hf	1.542	0.013	0.219
^{162}Ta	0.053	0.003	0.029	^{164}Hf	2.345	0.025	0.290
^{163}Ta	0.253	0.006	0.135	^{165}Hf	3.051	0.028	0.343
^{164}Ta	0.657	0.008	0.105	^{166}Hf	3.021	0.034	0.329
^{165}Ta	1.288	0.013	0.181	^{167}Hf	2.907	0.034	0.305
^{166}Ta	2.293	0.025	0.275	^{168}Hf	2.389	0.033	0.247
^{167}Ta	3.078	0.031	0.343	^{169}Hf	1.764	0.017	0.182
^{168}Ta	3.421	0.041	0.367	^{170}Hf	1.240	0.012	0.126
^{169}Ta	3.369	0.037	0.351	^{171}Hf	0.802	0.029	0.082
^{170}Ta	2.873	0.035	0.297	^{172}Hf	0.471	0.007	0.048

TABLE IX. Isotopic cross sections of spallation-evaporation residues of ^{238}U(1A GeV)+d, with their statistical and systematic uncertainties.

Nucleus	σ (mb)	ε_{STAT} (mb)	ε_{SYST} (mb)	Nucleus	σ (mb)	ε_{STAT} (mb)	ε_{SYST} (mb)
^{173}Hf	0.261	0.005	0.027	^{175}Lu	0.003	0.001	0.001
^{174}Hf	0.140	0.007	0.014	^{154}Yb	0.021	0.001	0.012
^{175}Hf	0.076	0.005	0.008	^{155}Yb	0.112	0.003	0.061
^{176}Hf	0.038	0.003	0.004	^{156}Yb	0.316	0.005	0.176
^{177}Hf	0.018	0.001	0.010	^{157}Yb	0.668	0.009	0.140
^{178}Hf	0.006	0.001	0.001	^{158}Yb	1.257	0.018	0.212
^{156}Lu	0.010	0.001	0.006	^{159}Yb	1.945	0.027	0.271
^{157}Lu	0.053	0.002	0.029	^{160}Yb	2.332	0.024	0.292
^{158}Lu	0.214	0.004	0.117	^{161}Yb	2.471	0.023	0.286
^{159}Lu	0.514	0.008	0.282	^{162}Yb	2.335	0.021	0.255
^{160}Lu	1.114	0.017	0.182	^{163}Yb	1.897	0.034	0.202
^{161}Lu	1.835	0.023	0.254	^{164}Yb	1.412	0.013	0.148
^{162}Lu	2.246	0.023	0.288	^{165}Yb	1.000	0.012	0.103
^{163}Lu	2.785	0.026	0.318	^{166}Yb	0.662	0.008	0.067
^{164}Lu	2.687	0.024	0.294	^{167}Yb	0.417	0.006	0.042
^{165}Lu	2.310	0.033	0.246	^{168}Yb	0.239	0.010	0.125
^{166}Lu	1.918	0.018	0.199	^{169}Yb	0.116	0.003	0.061
^{167}Lu	1.406	0.015	0.144	^{170}Yb	0.032	0.008	0.005
^{168}Lu	0.879	0.010	0.090	^{171}Yb	0.009	0.003	0.002
^{169}Lu	0.620	0.010	0.062	^{150}Tm	0.001	0.0003	0.0004
^{170}Lu	0.342	0.006	0.034	^{151}Tm	0.007	0.001	0.002
^{171}Lu	0.194	0.004	0.019	^{152}Tm	0.055	0.004	0.011
^{172}Lu	0.093	0.008	0.009	^{153}Tm	0.170	0.006	0.041
^{173}Lu	0.043	0.007	0.022	^{154}Tm	0.419	0.010	0.101
^{174}Lu	0.010	0.003	0.001	^{155}Tm	0.845	0.018	0.172

TABLE X. Isotopic cross sections of spallation-evaporation residues of ^{238}U(1A GeV)+d, with their statistical and systematic uncertainties.

Nucleus	σ (mb)	ε_{STAT} (mb)	ε_{SYST} (mb)	Nucleus	σ (mb)	ε_{STAT} (mb)	ε_{SYST} (mb)
^{156}Tm	1.409	0.024	0.230	^{160}Er	0.998	0.024	0.092
^{157}Tm	1.923	0.032	0.261	^{161}Er	0.665	0.019	0.062
^{158}Tm	2.136	0.038	0.258	^{162}Er	0.379	0.018	0.039
^{159}Tm	2.184	0.035	0.237	^{163}Er	0.214	0.009	0.031
^{160}Tm	1.947	0.034	0.199	^{164}Er	0.089	0.007	0.024
^{161}Tm	1.656	0.033	0.160	^{165}Er	0.028	0.004	0.018
^{162}Tm	1.169	0.026	0.111	^{146}Ho	0.004	0.001	0.002
^{163}Tm	0.880	0.023	0.081	^{147}Ho	0.032	0.002	0.018
^{164}Tm	0.539	0.023	0.050	^{148}Ho	0.105	0.005	0.065
^{165}Tm	0.346	0.013	0.031	^{149}Ho	0.267	0.009	0.095
^{166}Tm	0.178	0.011	0.019	^{150}Ho	0.524	0.013	0.165
^{167}Tm	0.077	0.008	0.016	^{151}Ho	1.012	0.019	0.221
^{168}Tm	0.019	0.003	0.014	^{152}Ho	1.505	0.024	0.247
^{148}Er	0.002	0.0004	0.001	^{153}Ho	1.660	0.027	0.235
^{149}Er	0.019	0.002	0.011	^{154}Ho	1.695	0.034	0.207
^{150}Er	0.081	0.005	0.020	^{155}Ho	1.594	0.030	0.172
^{151}Er	0.237	0.007	0.065	^{156}Ho	1.283	0.026	0.133
^{152}Er	0.539	0.011	0.135	^{157}Ho	0.970	0.024	0.104
^{153}Er	0.976	0.018	0.201	^{158}Ho	0.635	0.017	0.080
^{154}Er	1.497	0.023	0.244	^{159}Ho	0.409	0.013	0.068
^{155}Er	1.750	0.028	0.248	^{160}Ho	0.201	0.011	0.049
^{156}Er	1.885	0.036	0.232	^{161}Ho	0.115	0.005	0.046
^{157}Er	1.898	0.033	0.205	^{162}Ho	0.044	0.003	0.033
^{158}Er	1.670	0.031	0.169	^{144}Dy	0.008	0.001	0.004
^{159}Er	1.379	0.030	0.133	^{145}Dy	0.048	0.003	0.016

TABLE XI. Isotopic cross sections of spallation-evaporation residues of ^{238}U(1A GeV)+d, with their statistical and systematic uncertainties.

Nucleus	σ (mb)	ε_{STAT} (mb)	ε_{SYST} (mb)	Nucleus	σ (mb)	ε_{STAT} (mb)	ε_{SYST} (mb)
^{146}Dy	0.122	0.005	0.057	^{152}Tb	0.920	0.023	0.093
^{147}Dy	0.369	0.011	0.128	^{153}Tb	0.696	0.020	0.075
^{148}Dy	0.824	0.028	0.200	^{154}Tb	0.499	0.016	0.067
^{149}Dy	1.227	0.019	0.238	^{155}Tb	0.272	0.009	0.055
^{150}Dy	1.534	0.024	0.243	^{156}Tb	0.159	0.009	0.057
^{151}Dy	1.608	0.027	0.218	^{157}Tb	0.070	0.003	0.056
^{152}Dy	1.521	0.032	0.181	^{142}Gd	0.088	0.002	0.016
^{153}Dy	1.385	0.028	0.147	^{143}Gd	0.452	0.009	0.089
^{154}Dy	1.121	0.026	0.110	^{144}Gd	0.785	0.014	0.140
^{155}Dy	0.857	0.023	0.084	^{145}Gd	1.194	0.019	0.211
^{156}Dy	0.557	0.018	0.062	^{146}Gd	1.415	0.022	0.249
^{157}Dy	0.364	0.012	0.056	^{147}Gd	1.291	0.024	0.232
^{158}Dy	0.184	0.010	0.046	^{148}Gd	1.053	0.023	0.185
^{159}Dy	0.096	0.004	0.046	^{149}Gd	0.938	0.023	0.167
^{141}Tb	0.003	0.0004	0.001	^{150}Gd	0.685	0.020	0.124
^{142}Tb	0.018	0.002	0.007	^{151}Gd	0.484	0.016	0.093
^{143}Tb	0.063	0.003	0.029	^{152}Gd	0.354	0.014	0.072
^{144}Tb	0.176	0.006	0.086	^{153}Gd	0.193	0.009	0.072
^{145}Tb	0.429	0.013	0.161	^{154}Gd	0.163	0.009	0.052
^{146}Tb	0.876	0.035	0.220	^{155}Gd	0.113	0.006	0.054
^{147}Tb	1.403	0.021	0.247	^{156}Gd	0.065	0.005	0.040
^{148}Tb	1.526	0.024	0.232	^{157}Gd	0.062	0.005	0.030
^{149}Tb	1.530	0.027	0.199	^{139}Eu	0.019	0.001	0.004
^{150}Tb	1.419	0.031	0.161	^{140}Eu	0.160	0.004	0.031
^{151}Tb	1.262	0.034	0.129	^{141}Eu	0.441	0.009	0.084

TABLE XII. Isotopic cross sections of spallation-evaporation residues of ^{238}U(1A GeV)+d, with their statistical and systematic uncertainties.

Nucleus	σ (mb)	ε_{STAT} (mb)	ε_{SYST} (mb)	Nucleus	σ (mb)	ε_{STAT} (mb)	ε_{SYST} (mb)
^{142}Eu	0.898	0.015	0.165	^{137}Pm	0.648	0.012	0.133
^{143}Eu	1.182	0.019	0.207	^{138}Pm	1.072	0.017	0.223
^{144}Eu	1.318	0.021	0.231	^{139}Pm	1.217	0.020	0.228
^{145}Eu	1.242	0.023	0.222	^{140}Pm	1.145	0.020	0.255
^{146}Eu	1.104	0.024	0.198	^{141}Pm	1.020	0.019	0.252
^{147}Eu	0.768	0.020	0.138	^{132}Nd	0.030	0.001	0.019
^{148}Eu	0.599	0.018	0.128	^{133}Nd	0.176	0.004	0.054
^{149}Eu	0.419	0.014	0.120	^{134}Nd	0.413	0.007	0.102
^{150}Eu	0.302	0.012	0.099	^{135}Nd	0.798	0.013	0.172
^{151}Eu	0.199	0.009	0.079	^{136}Nd	0.980	0.016	0.227
^{152}Eu	0.157	0.007	0.083	^{137}Nd	1.113	0.018	0.272
^{153}Eu	0.099	0.005	0.073	^{138}Nd	1.063	0.019	0.292
^{137}Sm	0.063	0.002	0.012	^{139}Nd	1.009	0.020	0.283
^{138}Sm	0.263	0.006	0.050	^{140}Nd	0.857	0.018	0.270
^{139}Sm	0.680	0.012	0.131	^{141}Nd	0.753	0.017	0.281
^{140}Sm	1.061	0.018	0.191	^{130}Pr	0.083	0.002	0.028
^{141}Sm	1.352	0.022	0.249	^{131}Pr	0.216	0.004	0.071
^{142}Sm	1.377	0.024	0.237	^{132}Pr	0.387	0.007	0.135
^{143}Sm	1.278	0.024	0.221	^{133}Pr	0.628	0.010	0.208
^{144}Sm	0.937	0.020	0.204	^{134}Pr	0.750	0.012	0.285
^{145}Sm	0.601	0.015	0.195	^{135}Pr	0.838	0.014	0.288
^{146}Sm	0.377	0.011	0.181	^{136}Pr	0.848	0.015	0.358
^{147}Sm	0.247	0.009	0.169	^{129}Ce	0.306	0.005	0.122
^{134}Pm	0.021	0.001	0.016	^{130}Ce	0.476	0.008	0.181
^{135}Pm	0.088	0.002	0.039	^{131}Ce	0.696	0.011	0.283
^{136}Pm	0.399	0.008	0.090	^{132}Ce	0.822	0.013	0.323

[1] J. Pereira, J. Benlliure, E. Casarejos, P. Armbruster, M. Bernas, A. Boudard, S. Czajkowski, T. Enqvist, R. Legrain, S. Leray, B. Mustapha, M. Pravikoff, F. Rejmund, K.-H. Schmidt, C. Stéphan, J. Taieb, L. Tassan-Got, C. Volant, and W. Wlazlo, accepted in Phys. Rev. C.

[2] W. Wlazlo, T. Enqvist, P. Armbruster, J. Benlliure, M. Bernas, A. Boudard, S. Czajkowski, R. Legrain, S. Leray, B. Mustapha, M. Pravikoff, F. Rejmund, K.-H. Schmidt, C. Stéphan, J. Taieb, L. Tassan-Got, and C. Volant, Phys. Rev. Lett. **84**, 5736 (2000).

[3] T. Enqvist, W. Wlazlo, P. Armbruster, J. Benlliure, M. Bernas, A. Boudard, S. Czajkowski, R. Legrain, S. Leray, B. Mustapha, M. Pravikoff, F. Rejmund, K.-H. Schmidt, C. Stéphan, J. Taieb, L. Tassan-Got, and C. Volant, Nucl. Phys. **A686**, 481 (2001).

[4] T. Enqvist, P. Armbruster, J. Benlliure, M. Bernas, A. Boudard, S. Czajkowski, R. Legrain, S. Leray, B. Mustapha, M. Pravikoff, F. Rejmund, K.-H. Schmidt, C. Stéphan, J. Taieb, L. Tassan-Got, F. Vives, C. Volant, and W. Wlazlo, Nucl. Phys. **A703**, 435 (2002).

[5] F. Rejmund, B. Mustapha, P. Armbruster, J. Benlliure, M. Bernas, A. Boudard, J. P. Dufour, T. Enqvist, R. Legrain, S. Leray, K.-H. Schmidt, C. Stéphan, J. Taieb, L. Tassan-Got, and C. Volant, Nucl. Phys. **A683**, 540 (2001).

[6] J. Benlliure, P. Armbruster, M. Bernas, A. Boudard, J. P. Dufour, T. Enqvist, R. Legrain, S. Leray, B. Mustapha, F. Rejmund, K.-H. Schmidt, C. Stéphan, L. Tassan-Got, and C. Volant, Nucl. Phys. **A683**, 513 (2001).

[7] P. Armbruster, J. Benlliure, M. Bernas, A. Boudard, E. Casarejos, S. Czajkowski, T. Enqvist, S. Leray, P. Napolitani, J. Pereira, F. Rejmund, M.-V. Ricciardi, K.-H. Schmidt, C. Stéphan, J. Taieb, L. Tassan-Got, and C. Volant, Phys. Rev. Lett. **93**, 212701 (2004).

[8] J. Taieb, K.-H. Schmidt, L. Tassan-Got, P. Armbruster, J. Benlliure, M. Bernas, A. Boudard, E. Casarejos, S. Czajkowski, T. Enqvist, R. Legrain, S. Leray, B. Mustapha, F. Rejmund, C. Stéphan, C. Volant, and W. Wlazlo, Nucl. Phys. **A724**, 413 (2003).

[9] M. Bernas, P. Armbruster, J. Benlliure, A. Boudard, E. Casarejos, S. Czajkowski, T. Enqvist, R. Legrain, S. Leray, B. Mustapha, P. Napolitani, J. Pereira, F. Rejmund, M.-V. Ricciardi, K.-H. Schmidt, C. Stéphan, J. Taieb, L. Tassan-Got, C. Volant, and W. Wlazlo, Nucl. Phys. **A725**, 213 (2003).

[10] M. Bernas, P. Armbruster, J. Benlliure, A. Boudard, E. Casarejos, S. Czajkowski, T. Enqvist, R. Legrain, S. Leray, B. Mustapha, P. Napolitani, J. Pereira, F. Rejmund, M.-V. Ricciardi, K.-H. Schmidt, C. Stéphan, J. Taieb, L. Tassan-Got, C. Volant, and W. Wlazlo, Nucl. Phys. A **765**, 197 (2006).

[11] B. Fernandez-Dominguez, P. Armbruster, L. Audouin, J. Benlliure, M. Bernas, A. Boudard, E. Casarejos, S. Czajkowski, J. E. Ducret, T. Enqvist, B. Jurado, R. Legrain, S. Leray, B. Mustapha, J. Pereira, M. Pravikoff, F. Rejmund, M. V. Ricciardi, K.-H. Schmidt, C. Stephan, J. Taieb, L. Tassan-Got, and C. Volant, Nucl. Phys. **A747**, 227 (2005).

[12] C. Villagrasa, A. Boudard, J. E. Ducret, B. Fernandez, S. Leray, C. Volant, W. Wlazlo, P. Armbruster, T. Enqvist, F. Hammache, K. Helariutta, B. Jurado, M. V. Ricciardi, K.-H. Schmidt, K. Summerer, F. Vives, O. Yordanov, L. Audouin, L. Ferran, F. Rejmund, C. Stéphan, L. Tassan-Got, J. Benlliure, E. Casarejos, A. Fernandez, J. Pereira, S. Czajkowski, D. Karamanis, M. Pravikoff, J. George, R. A. Mewaldt, N. Yanazak, A. Wiedenbeck, J. Connel, T. Faestermann, A. Heinz, and A. Junghans, AIP Conf. Proc. **769**, 842 (2005).
[13] C. Rubbia et al., Rep. CERN-AT/95-44(ET), 1995.
[14] C. D. Bowman, Annu. Rev. Nucl. Part. Sci. **48**, 505 (1998).
[15] See e.g. the proceedings on the *6th Conference on Radioactive Nuclear Beams*, September 2003, Argonne, Illinois, USA. Nucl. Phys. A 746 (2004).
[16] R. Serber, Phys. Rev. **72**, 1114 (1947).
[17] R. Michel, R. Bodemann, H. Busemann, R. Daunke, M. Gloris, H.-J. Lange, B. Klug, A. Krins, I. Leya, M. Luepke, S. Neumann, H. Reinhardt, M. Schnatz-Buettgen, U. Herpers, Th. Schiekel, F. Sudbrock, B. Holmqvist, H. Conde, P. Malmborg, M. Suter, B. Dittrich-Hanne, P.-W. Kubik, H.-A. Synal, and D. Filges, Nucl. Instrum. Methods B **129**, 153 (1997).
[18] M. Gloris, R. Michel, F. Sudbrock, U. Herpers, P. Malmborg, and B. Holmqvist, Nucl. Instrum. Methods A **463**, 593 (2001).
[19] A. S. Goldhaber and H. H. Heckman, Annu. Rev. Nucl. Part. Sci. **28**, 161 (1978).
[20] P. Chesny, A. Forgeas, J. Gheller, G. Guiller, P. Pariset, L. Tassan-Got, P. Armbruster, K.-H. Behr, J. Benlliure, K. Burkard, A. Brünle, T. Enqvist, and F. Rejmund, GSI Annual Report 97-1, 1997, 190.
[21] A. Junghans, H.-G. Clerc, A. Grewe, M. de Jong, J. Mueller, and K.-H. Schmidt, Nucl. Instrum. Methods A **370**, 312 (1996).
[22] B. Jurado, K.-H. Schmidt, and K.-H. Behr, Nucl. Instrum. Methods A **483**, 603 (2002).
[23] H. Geissel, P. Armbruster, K.-H. Behr, A. Brünle, K. Burkard, M. Chen, H. Folger, B. Franczak, H. Keller, O. Klepper, B. Langenbeck, F. Nickel, E. Pfeng, M. Pfützner, E. Roeckl, K. Rykaczewsky, I. Schall, D. Schardt, C. Scheidenberger, K.-H. Schmidt, A. Schröter, T. Schwab, K. Sümmerer, M. Weber, G. Münzenberg, T. Brohm, H.-G. Clerc, M. Fauerbach, J.-J. Gaimard, A. Grewe, E. Hanelt, B. Knödler, M. Steiner, B. Voss, J. Weckenmann, C. Ziegler, A. Magel, H. Wollnik, J.-P. Dufour, Y. Fujita, D. J. Vieira, and B. Sherrill, Nucl. Instrum. Methods B **70**, 286 (1992).
[24] B. Voss, T. Brohm, H.-G. Clerc, A. Grewe, E. Hanelt, A. Heinz, M. de Jong, A. Junghans, W. Morawek, C. Roehl, S. Steinhäuser, C. Ziegler, K.-H. Schmidt, K.-H. Behr, H. Geissel, G. Münzenberg, F. Nickel, C. Scheidenberger, K. Sümmerer, A. Magel, and M. Pfützner, Nucl. Instrum. Methods A **364**, 150 (1995).
[25] M. Pfützner, H. Geissel, G. Münzenberg, F. Nickel, C. Scheidenberger, K.-H. Schmidt, K. Sümmerer, T. Brohm, B. Voss, and H. Bichsel, Nucl. Instrum. Methods B **86**, 213 (1994).
[26] J.-P. Dufour, R. Del Moral, H. Emmermann, F. Huber, D. Jean, C. Poinot, M. S. Pravikoff, A. Fleury, H. Delagrange, and K.-H. Schmidt, Nucl. Instrum. Methods A **248**, 267 (1986).
[27] J. Benlliure, K.-H. Schmidt, D. Cortina-Gil, T. Enqvist, F. Farget, A. Heinz, A. R. Junghans, J. Pereira, and J. Taieb, Nucl. Phys. **A660**, 87 (1999).
[28] J. Benlliure, J. Pereira-Conca, and K.-H. Schmidt, Nucl. Instrum. Methods A **478**, 493 (2002).
[29] C. Scheidenberger, Th. Stöhlker, W. E. Meyerhof, H. Geissel, P. H. Mokler, and B. Blank, Nucl. Instrum. Methods B **142**, 441 (1998).
[30] P. J. Karol, Phys. Rev. C **11**, 1203 (1975).
[31] T. Brohm and K.-H. Schmidt, Nucl. Phys. **A569**, 821 (1994).
[32] Th. Rubehn, W. F. J. Müller, R. Bassini, M. Begemann-Blaich, Th. Blaich, A. Ferrero, C. Gross, G. Imme, I. Iori, G. J. Kunde, W. D. Kunze, V. Lindenstruth, U. Lynen, T. Möhlenkamp, L. G. Moretto, B. Ocker, J. Pochodzalla, G. Raciti, S. Reito, H. Sann, A. Schüttauf, W. Seidel, V. Serfling, W. Trautmann, A. Trizcinski, G. Verde, A. Wörner, E. Zude, and B. Zwieglinski, Z. Phys. A **353**, 197 (1995).
[33] K.-H. Schmidt, S. Steinhäuser, C. Böckstiegel, A. Grewe, A. Heinz, A. R. Junghans, J. Benlliure, H.-G. Clerc, M. de Jong, J. Müller, M. Pfützner, and B. Voss, Nucl. Phys. **A665**, 221 (2000).
[34] J.-J. Gaimard and K.-H. Schmidt, Nucl. Phys. **A531**, 709 (1991).
[35] Nucl. Phys. **A629**, 635 (1998).
[36] P. Napolitani, L. Tassan-Got, P. Armbruster, and M. Bernas, Nucl. Phys. **A727**, 120 (2003).
[37] B. Mustapha, Ph.D. thesis at Universite de Paris Sud and U.F.R., Scientifique d'Orsay, France, 1998.
[38] M. V. Ricciardi, A. V. Ignatyuk, A. Kelic, P. Napolitani, F. Rejmund, K.-H. Schmidt, and O. Yordanov, Nucl. Phys. **A733**, 299 (2004).
[39] A. R. Junghans, M. de Jong, H.-G. Clerc, A. V. Ignatyuk, G. A Kudyaev, and K.-H. Schmidt, Nucl. Phys. **A629**, 635 (1998).
[40] J. P. Dufour, H. Delagrange, R. Del Moral, A. Fleury, F. Hubert, Y. Llabador, M. B. Mauhourat, K.-H. Schmidt, and A. Lleres, Nucl. Phys. **A387**, 157 (1982).
[41] J. B. Cumming, P. E. Haustein, R. W. Stoenner, L. Mausner, and R. A. Naumann, Phys. Rev. C **10**, 739 (1974).
[42] K. Sümmerer and B. Blank, Phys. Rev. C **61**, 034607 (2000).
[43] K.-H. Schmidt, M. V. Ricciardi, A. S. Botvina, and T. Enqvist, Nucl. Phys. **A710**, 157 (2002).
[44] J. Benlliure, E. Casarejos, J. Pereira, and K.-H. Schmidt, Phys. Rev. C **74**, 014609 (2006).
[45] E. Hanelt, Ph.D. thesis presented at TU Darmstadt, Institut für Kernphysik, Darmstadt, Germany, December 1991. Published also as GSI report GSI-92-05, 1992. Software tool available at http://www-w2k.gsi.de/charms/software.htm
[46] D. J. Morrissey, Phys. Rev. C **39**, 460 (1989).
[47] M. V. Ricciardi, T. Enqvist, J. Pereira, J. Benlliure, M. Bernas, E. Casarejos, V. Henzl, A. Kelic, J. Taieb, and K.-H. Schmidt, Phys. Rev. Lett. **90**, 212302 (2003).
[48] A. S. Goldhaber, Phys. Lett. **B53**, 306 (1974).
[49] E. Hanelt, A. Grewe, K.-H. Schmidt, T. Brohm, H.-G. Clerc, M. Dornik, M. Fauerbach, H. Geissel, A. Magel, G. Münzenberg, F. Nickel, M. Pfützner, C. Scheidenberger, M. Steiner, K. Sümmerer, B. Voss, M. Weber, J. Weckenmann, and C. Ziegler, Z. Phys. A **346**, 43 (1993).